CrossMark

The Lyα Reference Sample. VIII. Characterizing Lyα Scattering in Nearby Galaxies

Joanna S. Bridge[1,2,3,4] , Matthew Hayes[3] , Jens Melinder[3] , Göran Östlin[3] , Caryl Gronwall[1,2] , Robin Ciardullo[1,2] ,
Hakim Atek[5] , John M. Cannon[6] , Max Gronke[7] , Lucia Guaita[8] , Alex Hagen[1,2,9] , Edmund Christian Herenz[3] ,
Daniel Kunth[5] , Peter Laursen[7] , J. Miguel Mas-Hesse[10] , and Stephen A. Pardy[11]
[1] Department of Astronomy & Astrophysics, The Pennsylvania State University, University Park, PA 16802, USA; joanna.bridge@louisville.edu
[2] Institute for Gravitation and the Cosmos, The Pennsylvania State University, University Park, PA 16802, USA
[3] Department of Astronomy, Oskar Klein Centre, Stockholm University, AlbaNova University Centre, Stockholm, Sweden
[4] Department of Physics and Astronomy, 102 Natural Science Building, University of Louisville, Louisville KY 40292, USA
[5] Institut d Astrophysique de Paris, 98 bis Bd Arago, F-75014 Paris, France
[6] Department of Physics & Astronomy, Macalester College, Saint Paul, MN 55105, USA
[7] Institute of Theoretical Astrophysics, University of Oslo, Postboks 1029 Blindern, NO-0315 Oslo, Norway
[8] INAF-Osservatorio Astronomico di Roma, Via Frascati 33, I-00078, Monte Porzio Catone, Italy
[9] vizual.ai, 3600 O'Donnell Street, Suite 250, Baltimore, MD 21224, USA
[10] Centro de Astrobiología (CSIC INTA), Departamento de Astrofísica, PO Box 78, E-28691 Villanueva de la Cañada, Spain
[11] Department of Astronomy, University of Wisconsin—Madison, Madison, WI 53706, USA

Abstract

We examine the dust geometry and Lyα scattering in the galaxies of the Lyman Alpha Reference Sample (LARS), a set of 14 nearby ($0.02 < z < 0.2$) Lyα-emitting and starbursting systems with *Hubble Space Telescope* Lyα, Hα, and Hβ imaging. We find that the global dust properties determined by line ratios are consistent with other studies, with some of the LARS galaxies exhibiting clumpy dust media, while others of them show significantly lower Lyα emission compared to their Balmer decrement. With the LARS imaging, we present Lyα/Hα and Hα/Hβ maps with spatial resolutions as low as ∼40 pc, and use these data to show that in most galaxies, the dust geometry is best modeled by three distinct regions: a central core where dust acts as a screen, an annulus where dust is distributed in clumps, and an outer envelope where Lyα photons only scatter. We show that the dust that affects the escape of Lyα is more restricted to the galaxies' central regions, while the larger Lyα halos are generated by scattering at large radii. We present an empirical modeling technique to quantify how much Lyα scatters in the halo, and find that this "characteristic" scattering distance correlates with the measured size of the Lyα halo. We note that there exists a slight anti-correlation between the scattering distance of Lyα and global dust properties.

Key words: galaxies: ISM – galaxies: starburst – radiative transfer – scattering

1. Introduction

Ever since the question was posed of how distant galaxies could be detected, the Lyα emission line resulting from the $n = 2$ to $n = 1$ transition of hydrogen at 1216 Å has been recognized as key to studying high-redshift star-forming galaxies (Partridge & Peebles 1967). Lyα reprocesses approximately two-thirds of the ionizing photons from hot, massive, short-lived stars (Spitzer 1978). It is therefore expected to be the brightest emission line from young stellar populations (e.g., Raiter et al. 2010).

However, due to the high absorption cross-section between the $n = 1$ and $n = 2$ state, the neutral gas reservoirs in a galaxy lead to a complicated resonant radiative transfer problem. This process increases the path lengths that Lyα photons have to travel before escaping the galaxy, and therefore also increases the chance of being absorbed by interstellar dust grains (e.g., Neufeld 1990; Verhamme et al. 2006; Laursen et al. 2013; Behrens et al. 2014; Dijkstra 2014). The result is that Lyα is not observed in all star-forming galaxies, and in galaxies where it is observed, the sites of escaping emission and intrinsic production are different. Many factors govern the visibility of Lyα, such as kinematics, the porosity and clumpiness of the interstellar medium (ISM), and scattering (Kunth et al. 1994; Lequeux et al. 1995; Kunth et al. 1998; Mas-Hesse et al. 2003; Heckman et al. 2011; Wofford et al. 2013).

Nevertheless, Lyα has been used to find tens of thousands of high-redshift galaxies and, with the advent of experiments such as the Hobby Eberly Telescope Dark Energy Experiment (HETDEX; Hill et al. 2008) and *James Webb Space Telescope* (*JWST*; Gardner et al. 2006), it will remain the prime tracer of galaxy formation and evolution in the next decade. Therefore, it is of paramount importance that the processes by which Lyα is emitted from galaxies are very well understood. This requires understanding Lyα radiative transfer on small scales.

One of the best samples in which to study resolved Lyα is the Lyman Alpha Reference Sample (LARS; Hayes et al. 2013, 2014; Östlin et al. 2014; Pardy et al. 2014; Rivera-Thorsen et al. 2015; Duval et al. 2016; Herenz et al. 2016). The LARS sample comprises 14 nearby ($0.02 < z < 0.2$) Lyα-emitting and/or absorbing galaxies with extensive *Hubble Space Telescope* (*HST*) broadband and narrowband imaging, supplemented by observations from numerous other telescopes. The goal of these observations is to probe exactly how the Lyα photons travel and by what mechanism they escape. The work presented here will use this unique sample of galaxies to model the behavior of dust and Lyα scattering in star-forming galaxies.

One way to understand what Lyα tells us about a galaxy is to compare it to the very well understood transition of Hα, the H I Balmer transition from $n = 3$ to $n = 2$ at 6563 Å (e.g., Hayes et al. 2007; Östlin et al. 2009; Herenz et al. 2016). In star-forming galaxies, Balmer emission serves as a proxy for the
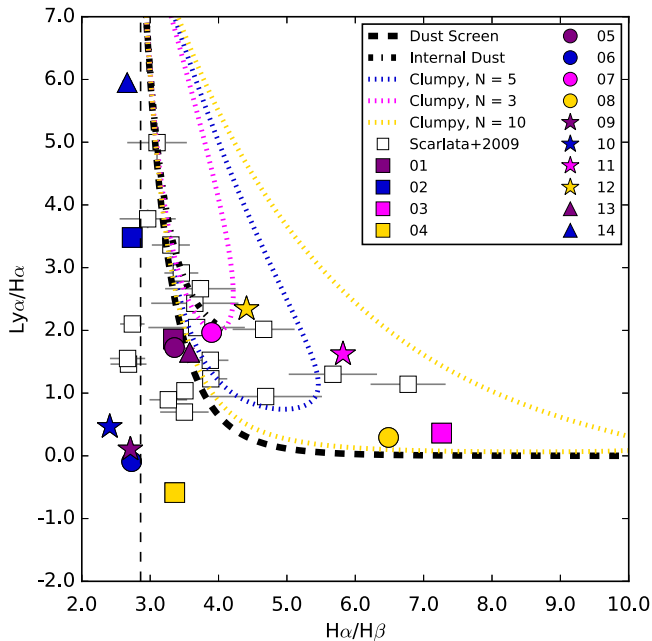
Figure 1. Lyα/Hα vs. Hα/Hβ for the 14 LARS galaxies. The various curves denote different dust geometry models. A simple uniform dust screen is shown as a black dashed line, while a smooth internal dust model is shown with a black dashed-dotted line. The blue, magenta, and yellow dotted lines show a clumpy dust model for different numbers of clumps along the line of sight (N). Moving counter-clockwise along the curves corresponds to higher optical depths of the dust. For most of the galaxies, the error bars ($\pm 1\sigma$ assuming a normal distribution) are within the plot markers. Shown for comparison are the $z \sim 0.3$ *GALEX* LAEs from Scarlata et al. (2009). The vertical dashed black line shows the intrinsic Balmer decrement value of Hα/Hβ = 2.86.

total ionizing flux of the stars embedded in the galaxies, and is therefore one of the more direct ways (when corrected for reddening) to quantify a system's current star formation (Kennicutt 1998). The same recombination events that generate Lyα photons also generate Hα, meaning that Hα traces Lyα but without the complicated radiative transfer of resonance. The comparison of Lyα and Hα is therefore a way of understanding what we are missing when we focus only on the Lyα emission. This is particularly useful because the reason that high-redshift galaxies are studied in Lyα is because their Hα emission is shifted out of the optical (and near-infrared for $z > 2.5$) and is therefore often unavailable. If we are able to quantify what information is missed by the complicated radiative transfer of Lyα compared to Hα, we can then use that knowledge in high-redshift galaxy studies.

In this work, we use the Hα and Hβ emission of the LARS galaxies to simulate their Lyα emission to obtain a characteristic scattering distance for Lyα photons, and show how dust geometry creates deviations from a simple scattering model. We summarize the LARS data set and reductions in Section 2. In Section 3, we perform spatially resolved analysis of Hα/Hβ and Lyα/Hα emission line ratios to pinpoint mechanisms for the escape of Lyα photons. We describe how Hα observations can be used to create simulated Lyα distributions in order to obtain a characteristic scattering distance for each galaxy in Section 4. We discuss the implications of this study in Section 5, and conclude with Section 6, describing how this work can be expanded upon in the future.

In this work, we adopt the standard ΛCDM cosmology, with $H_0 = 70$ km s^{-1} Mpc^{-1}, $\Omega_M = 0.3$, and $\Omega_\Lambda = 0.7$ (Komatsu et al. 2011).

2. Data

The 14 LARS galaxies were chosen from the *GALEX* General Release 2 and SDSS Data Release 6 catalogs. The galaxies were chosen to have Hα equivalent widths of $EW_{H\alpha} > 100$ Å, ensuring a sample with significant active star formation and Lyα photon production. The sample is bright in both the far-UV ($16.6 < m_{FUV} < 19.2$) and near-UV ($16.2 < m_{NUV} < 19.1$) and has a far-UV luminosity range of $9.2\,L_\odot < \log(L_{FUV}) < 10.7\,L_\odot$. These luminosities are on par with higher-redshift Lyα emitters and Lyman break galaxies (LBGs), making the LARS sample a set of reasonable high-redshift analog galaxies. For further sample details, see Östlin et al. (2014; Tables 1–3 therein.) While the details of the data set and data reduction can also be found in Hayes et al. (2013) and Östlin et al. (2014), we summarize the procedures here.

2.1. Observations

The LARS galaxies were imaged by the *HST* using a synthetic narrowband centered on Lyα. The technique used to measure the Lyα emission line is described in detail in Östlin et al. (2014) and Hayes et al. (2009). Briefly, a synthetic narrowband image was created by subtracting the F140LP and F150LP or the F125LP and F140LP long-pass filters (depending on the galaxy redshift) on the Solar Blind Channel to observe the Lyα line. Either the Wide Field Camera 3 (WFC3) or the Advanced Camera for Surveys (ACS) were then used to obtain Hα and Hβ emission maps. These three emission maps serve as the basis for our following analysis.

2.2. Data Processing

The images were reduced using the `Drizzlepac`[12] package in the standard *HST* reduction algorithm. We used custom-built software called Lyα Extraction Software (`LaXs`; Hayes et al. 2009; Östlin et al. 2014) to subtract the continuum from the Lyα images. To find the underlying continuum flux in Lyα (and to lesser extent Hα and Hβ), we performed spectral energy distribution fitting using observations from five continuum filters on *HST* (two in the far-UV (FUV) and three in the optical). To briefly summarize: we fit each pixel with a three-component model, comprised of a young, star-forming population, a stellar continuum from older stars, and line+continuum produced by photoionization. These were fit to the data with a χ^2 fitting method and population spectra from `Starburst99` templates (Leitherer et al. 1999). The free parameters in this procedure are the equivalent width of the Lyα line, the age (of the young population), $E(B-V)_s$, and the masses of the young and old populations. The fitting routine also accounts for flux from the nebular continuum by utilizing the Hα and Hβ observations. For more details see Hayes et al. (2009). The images' point spread functions were also matched using custom-made software (Hayes et al. 2016; J. Melinder et al. 2017, in preparation).

2.3. Photometric Analysis

Using the appropriate aperture for each galaxy is important, as we need to determine a size that encompasses as much of the Lyα emission as possible without including too much background. The Petrosian (1976) radius determined from the UV

---

[12] http://drizzlepac.stsci.edu/

Table 1
LARS Integrated Fluxes

LARS ID	z	Lyα (erg s^{-1} cm^{-2})	Hα (erg s^{-1} cm^{-2})	Hβ (erg s^{-1} cm^{-2})
01	0.028	$(5.25 \pm 0.03) \times 10^{-13}$	2.82×10^{-13}	8.44×10^{-14}
02	0.030	$(2.56 \pm 0.01) \times 10^{-13}$	7.36×10^{-14}	2.69×10^{-14}
03	0.031	$(9.87 \pm 0.07) \times 10^{-14}$	2.72×10^{-13}	3.75×10^{-14}
04	0.033	$(-1.12 \pm 0.01) \times 10^{-13}$	1.91×10^{-13}	5.67×10^{-14}
05	0.034	$(2.75 \pm 0.02) \times 10^{-13}$	1.60×10^{-13}	5.76×10^{-14}
06	0.034	$(-2.30 \pm 0.45) \times 10^{-15}$	2.48×10^{-14}	9.11×10^{-15}
07	0.038	$(2.30 \pm 0.02) \times 10^{-13}$	1.17×10^{-13}	3.00×10^{-14}
08	0.038	$(1.01 \pm 0.01) \times 10^{-13}$	3.44×10^{-13}	5.31×10^{-14}
09	0.047	$(4.58 \pm 0.16) \times 10^{-14}$	4.33×10^{-13}	1.60×10^{-13}
10	0.057	$(1.56 \pm 0.05) \times 10^{-14}$	3.37×10^{-14}	1.40×10^{-14}
11	0.084	$(1.47 \pm 0.00) \times 10^{-13}$	9.06×10^{-14}	1.56×10^{-14}
12	0.102	$(1.71 \pm 0.01) \times 10^{-13}$	7.28×10^{-14}	1.65×10^{-14}
13	0.147	$(6.78 \pm 2.68) \times 10^{-14}$	4.11×10^{-14}	1.15×10^{-14}
14	0.181	$(1.63 \pm 0.00) \times 10^{-13}$	2.75×10^{-14}	1.03×10^{-14}

continuum does not encompass the outer regions of the Lyα halo for every galaxy. We therefore created an aperture by convolving the UV continuum image with a $\sigma = 50$ pixel Gaussian kernel, creating a larger aperture. Using this convolved image, we calculated an isophotal radius at which the local intensity is 20% of the average flux contained within the radius, and used this radius to define the aperture for each galaxy. However, in cases where the Lyα halo morphology is particularly extended or more complex, even this radius is not large enough to encompass all of the Lyα emission. For LARS01, LARS02, LARS05, LARS07, and LARS08, we therefore used 1.5 times this radius to define the aperture to include all of the Lyα emission from the galaxy. Using an isophotal measurement of the radius, rather than a fixed circular aperture, maximizes the signal while decreasing the background. The aperture is large enough to contain the extended Lyα emission while excluding excess background. An average of 75% of the Lyα emission is captured within the calculated apertures.

3. Emission Line Ratios and Dust Geometry

Intrinsically, the ratio of Lyα to Hα in Case B nebulae with $T = 5000$–$20,000$ K and $n_e = 10^2 - 10^4$ cm^{-3} varies from 8.1 to 11.6 (Hummer & Storey 1987). Convention dictates that, roughly, Lyα/H$\alpha \sim 8.7$ (Hu et al. 1998; Hayes 2015). Deviations from this ratio capture the physics of Lyα radiative transfer as well as information about the dust extinction, while departures from Hα/H$\beta = 2.86$ can be used to probe the dust content of a galaxy (Pengelly 1964; Brocklehurst 1971). Therefore, we use the Lyα and Hα emission maps to calculate these ratios for the LARS galaxies, giving insight into the radiation physics, dust geometry, and reddening in galaxies.

3.1. Integrated Emission Lines

In Figure 1, we show the integrated line ratios for the 14 LARS galaxies, with the fluxes given in Table 1. Following Scarlata et al. (2009), we show several models describing dust geometry. A simple dust screen model with $R_V = 3.07$ (Cardelli et al. 1989) is denoted by the black dashed line. The black dashed-dotted line demonstrates a smooth internal dust model (Mathis 1972), where the stars, gas, and dust are evenly mixed. This model is described as $I_\lambda/I_\lambda^0 = (1 - e^{-\tau_\lambda})/\tau_\lambda$, where I_λ is

the observed intensity of the source, I_λ^0 is the assumed intrinsic intensity, and τ_λ is the optical depth of the medium. Finally, we show models for various clumpy media following the formalism of Natta & Panagia (1984),

$$\frac{I_\lambda}{I_\lambda^0} = \exp(-N(1 - e^{-\tau_{c,\lambda}})), \qquad (1)$$

where I_λ and I_λ^0 are defined as before, N is the mean number of clumps along the line of sight, and $\tau_{c,\lambda}$ is the optical depth of each clump. The number of clumps per sightline follow a Poisson distribution and individually obey the Cardelli model, with each clump having the same optical depth. These models do not include Lyα radiative transfer effects. Scarlata et al. (2009) found that a majority of $z \sim 0.3$ Lyα emitting galaxies were best described by the clumpy dust model. Meanwhile, for the galaxies that lie below the uniform dust screen model, they noted that a mechanism that would preferentially dampen the Lyα photons but leave the Balmer photons unaffected would be required, such as a neutral medium through which the Lyα photons would pass without scattering.

We find that while several of the LARS galaxies lie in the region of Figure 1 described by a clumpy dust model, others show Lyα to be significantly lower than that inferred from the Balmer decrement. Of particular note are the galaxies for which the Hα/Hβ ratios are consistent with the intrinsic value, but have Lyα/Hα values anywhere from $\sim$75% (LARS14) to nearly 100% (LARS09) less than than the intrinsic value of 8.7. This is in agreement with previous studies that have found that integrated Lyα emission is often much weaker than expected from recombination theory (e.g., Terlevich et al. 1993; Giavalisco et al. 1996; Atek et al. 2008; Scarlata et al. 2009). Overall, the LARS galaxies show Lyα/Hα ratios that span the whole range from no additional destruction of photons beyond that done by dust to the formation of damped Lyα absorption profiles.

The internal dust model is difficult to differentiate from a clumpy dust model at low optical depth and a small number of clumps. However, given the global values shown in Figure 1, it is unlikely that the internal dust best explains the ISM in the LARS galaxies.
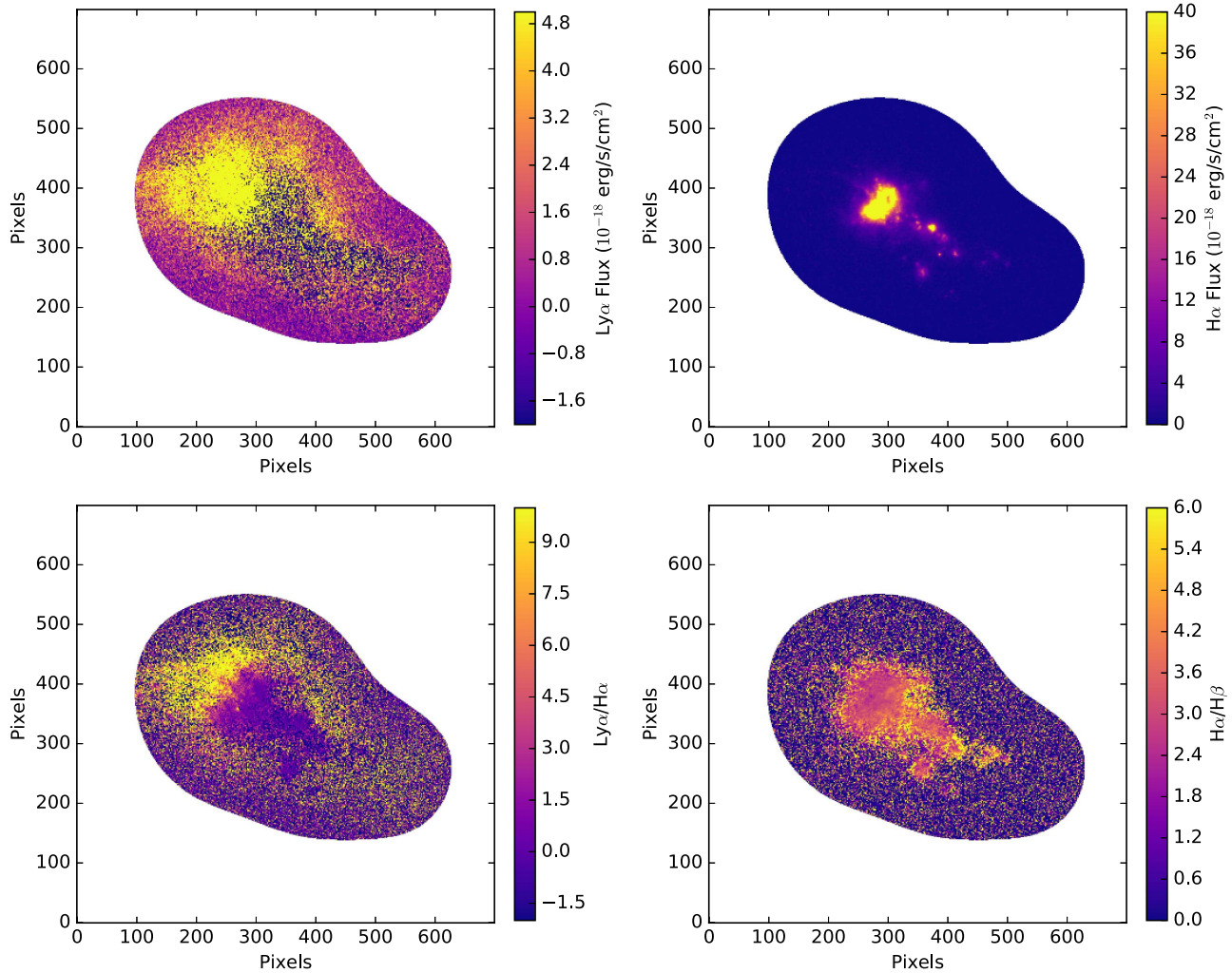
Figure 2. Images of LARS01. The calculated aperture has been applied. Top left: the Lyα emission map. Top right: the Hα emission map. Bottom left: the Lyα/Hα ratio, with an average uncertainly of 0.01. Bottom right: the Hα/Hβ ratio with an average uncertainly of 0.001.

3.2. Resolved Emission Line Ratios

Using the resolved line maps of the LARS galaxies, we are able to probe the dust geometry down to the minimum physical scales allowed by the *HST* point spread function (see J. Melinder et al. 2017, in preparation), which for these galaxies is approximately 40 to 130 parsecs, depending on redshift. By using the emission line ratios and knowing where exactly in the galaxies different line ratios occur, we can trace what regions in the galaxies are affecting the integrated line ratios. In this section, we will compare two galaxies that are each representative of differing dust models, LARS01 and LARS12. The *HST* Lyα and Hα emission maps are shown for these two galaxies in top panels of Figures 2 and 3, respectively. Because the Hβ images have low signal-to-noise in the outer regions of the galaxies, we have implemented a cut in the Hβ line maps of $f_{H\beta} = 1 \times 10^{-18}$ erg/s/cm². We then use only the pixels from all three emission maps that correspond to Hβ values greater than this cut.

LARS01, which is displayed in Figure 1 as a purple square, is an example of a galaxy that is not well described by a clumpy dust model. We show the Lyα/Hα versus Hα/Hβ values for the galaxy in Figure 4. As in Figure 1, we have plotted the various dust models. While some pixels fall in the clumpy

model region, most lie below the plotted dust models. Scarlata et al. (2009) noted that the dust models shift slightly downwards if the scattering of Lyα photons *within* the clumps is included. This effectively increases the optical depth of these photons. Further dampening of Lyα may be due to these photons traveling through the neutral hydrogen in the ISM. Additionally, a number of pixels correspond to regions where the Lyα is the same or brighter than predicted by recombination physics. In the lower panels of Figure 2, the Lyα/Hα and Hα/Hβ ratios are shown for the galaxy.

In addition to the bright Lyα, there are also a significant number of pixels that have Lyα/Hα < 0. Some of these may be due to noise, producing artificially negative Lyα values. Nevertheless, our cut in Hβ minimizes the number of pixels affected by noise. Therefore, the negative Lyα/Hα values are more likely to be where Lyα is seen in absorption. This is due to continuum light being either absorbed or scattered by the $n = 2$ to $n = 1$ resonance. The Lyα emission maps shown in the top right panels of Figures 2 and 3 display the negative Lyα pixels in dark purple. The fact that the negative pixels are spatially correlated, particularly in the more central regions of the galaxies, indicates that these are real absorption features.

Unlike LARS01, LARS12, denoted in Figure 1 by a yellow star, falls directly in the region of the clumpy dust models. We

show the Lyα/Hα versus Hα/Hβ values for the pixels in LARS12, along with the same dust models, in Figure 5. As would be expected from the global Lyα/Hα and Hα/Hβ ratios, a majority of the pixels fall in the regions of the plot well described by the clumpy dust models with varying N (numbers of clumps along the line of sight) and τ (optical depth). Overall, LARS12 has much higher Hα/Hβ values than LARS01, indicating that the galaxy is significantly dustier. We show the Lyα/Hα and Hα/Hβ ratios of LARS12 in the bottom panels of Figure 3.

To quantify the comparison of Lyα and Hα in a galaxy, we examine their respective surface brightnesses (Östlin et al. 2009). We plot the surface photometry for LARS01 in the left panel of Figure 6. Shown in black are the logarithmic Lyα surface brightnesses plotted against the logarithmic Hα surface brightnesses. The solid red line indicates the intrinsic Lyα/Hα ~ 8.7 expected under the assumption of Case B recombination. Lower Lyα/Hα ratios indicate either dust absorption or scattering of the Lyα photons out of the line of sight, while Lyα/Hα values greater than ~ 8.7 show where Lyα has likely been scattered *into* the line of sight.

Overplotted in blue in the left panel of Figure 6 are the individual pixels of LARS01 that fall in the region corresponding to the clumpy dust models of Natta & Panagia (1984; defined as any pixel lying above the dust screen curve in Figure 4). Most of the blue pixels show Lyα/Hα ratios well below the intrinsic relationship, indicating that the Lyα photons are either absorbed by dust or scattered out of the line of sight by neutral hydrogen (Hayes 2015). Some pixels indicate that Lyα photons have also been scattered into the line of sight, as they are overluminous for the corresponding Hα surface brightnesses. Both of these scenarios can be explained by the presence of a clumpy medium that can both dampen as well as scatter the Lyα. The brightest Lyα pixels (in the upper right region of the left panel of Figure 6) are not affected by the clumpy medium.

In the center panel of Figure 6, we trace the pixels in the clumpy dust region of Figure 4 back to the LARS01 Lyα image. What is immediately obvious is that the Lyα photons that are escaping from the center of the galaxy are *not* doing so through a clumpy dust medium. Not only is the central ~ 0.65 kpc diameter region the source of the brightest Lyα emission, but its Hα/Hβ ratio is very close to the intrinsic value of 2.86. Whatever minimal extinction exists in the region is consistent with that expected from a dust screen model. This suggests that the region has been cleared of static neutral hydrogen, either by the winds from a preponderance of supernovae or by a bubble blown out by the region's active star formation. The resulting outflows then allow Lyα photons in the wings of the line to escape (Mas-Hesse et al. 2003; Rivera-Thorsen et al. 2015; Herenz et al. 2016). Moreover, the concentration of ionized hydrogen in the galaxy's central region (see Figure 2) indicates that most of the medium has been ionized, and is therefore transparent to Lyα photons. Laursen et al. (2009) showed that the dust model used in Lyα radiative transfer calculations is relatively unimportant, as the photons either travel through fairly dust-free regions, or they travel through dusty regions and are absorbed. This is in line with the general lack of Lyα attenuation in the center of LARS01.

Most of the pixels that lie above the Cardelli et al. (1989) dust screen model in Figure 4 come from a concentrated annular region around the center of the galaxy. This indicates that an annulus of clumpy dust exists outside the central star-forming region.

Rivera-Thorsen et al. (2015) observed the LARS galaxies using the Cosmic Origin Spectrograph (COS) on the *HST*. They found that, in general, gas outflows with velocities greater than 50 km s^{-1} occurred in all of the galaxies where Lyα is observed. The model used to explain this behavior (Tenorio-Tagle et al. 1999; Mas-Hesse et al. 2003) posits that feedback from the actively star-forming regions in the center of the galaxy creates Rayleigh–Taylor instabilities at the border between the hot bubble and the neutral phase of the ISM. This results in a clumpy medium through which Lyα photons can either escape or be absorbed. This model could explain the regions we observe in LARS01 and the other LARS galaxies.

In contrast to LARS01, the integrated ratios of LARS12 place it solidly in the region of Figure 1 that is described by the clumpy dust models. LARS12 is consistent with the clumpy dust model almost all the way to the nucleus (see Figure 7). While Lyα escapes freely from the inner ~ 0.65 kpc of LARS01, the same cavity in LARS12 is only ~ 0.4 kpc in diameter. This region is denoted by several pixels in the center of the galaxy, shown in the center panel of Figure 7. This difference can also be seen in the curve of growth analysis performed by Hayes et al. (2014; Figure 4): in LARS01, the integrated Lyα flux peaks close to the galactic center, while in LARS12, this peak is 5 kpc from the galaxy's center. In other words, in the center of LARS12, dust attenuation is suppressing Lyα emission in the center of LARS12 compared to what would be expected from a clumpy dust medium.

We next isolate the pixels of the LARS01 image that fall *above* the intrinsic Lyα/Hα value. The regions of the galaxy in which these pixels are located are of particular interest as they provide insight into the mechanisms that can transport Lyα to large radii. Previous studies have found that in some galaxies, as much as 70% of the Lyα emission comes from the diffuse regions that are outside the more central areas of star formation (Hayes et al. 2005; Atek et al. 2008). These halos often reach galactocentric radii of 10 kpc. Several processes can theoretically modify the Lyα/Hα ratio, such as extreme high or low densities, shocks, and other non-equilibrium conditions, but the more likely explanation of an upward deviation from Lyα/Hα ~ 8.7 is the physics of Lyα radiative transfer (e.g., Hayes 2015). The fact that Lyα/Hα $\gg 10$ is frequently observed tells us that scattering into the line of sight not only happens, but that it can dominate the integrated luminosity of a galaxy.

In the right panel of Figure 6, we show only the regions of LARS01 where Lyα photons are scattered into the line of sight. The pixels that contain overly bright Lyα make up the Lyα halo of LARS01. Figure 7 shows the same quantity but for LARS12. This galaxy has the same characteristics as LARS01, with the highest Lyα/Hα pixels being the most significant contributor to the emission from the outer halo. For Lyα photons to be this bright relative to Hα, the photons have to be *scattered* into the line of sight. It has been shown that the size of extended Lyα halos around low-redshift Lyα emitters is inversely correlated with dust content, indicating that low dust abundance is necessary for Lyα photons to resonantly scatter to large radii (Hayes et al. 2013). The fact that the high Lyα/Hα pixels correspond directly to the Lyα halo indicates that the halo is generated by a scattering process where little dust exists,
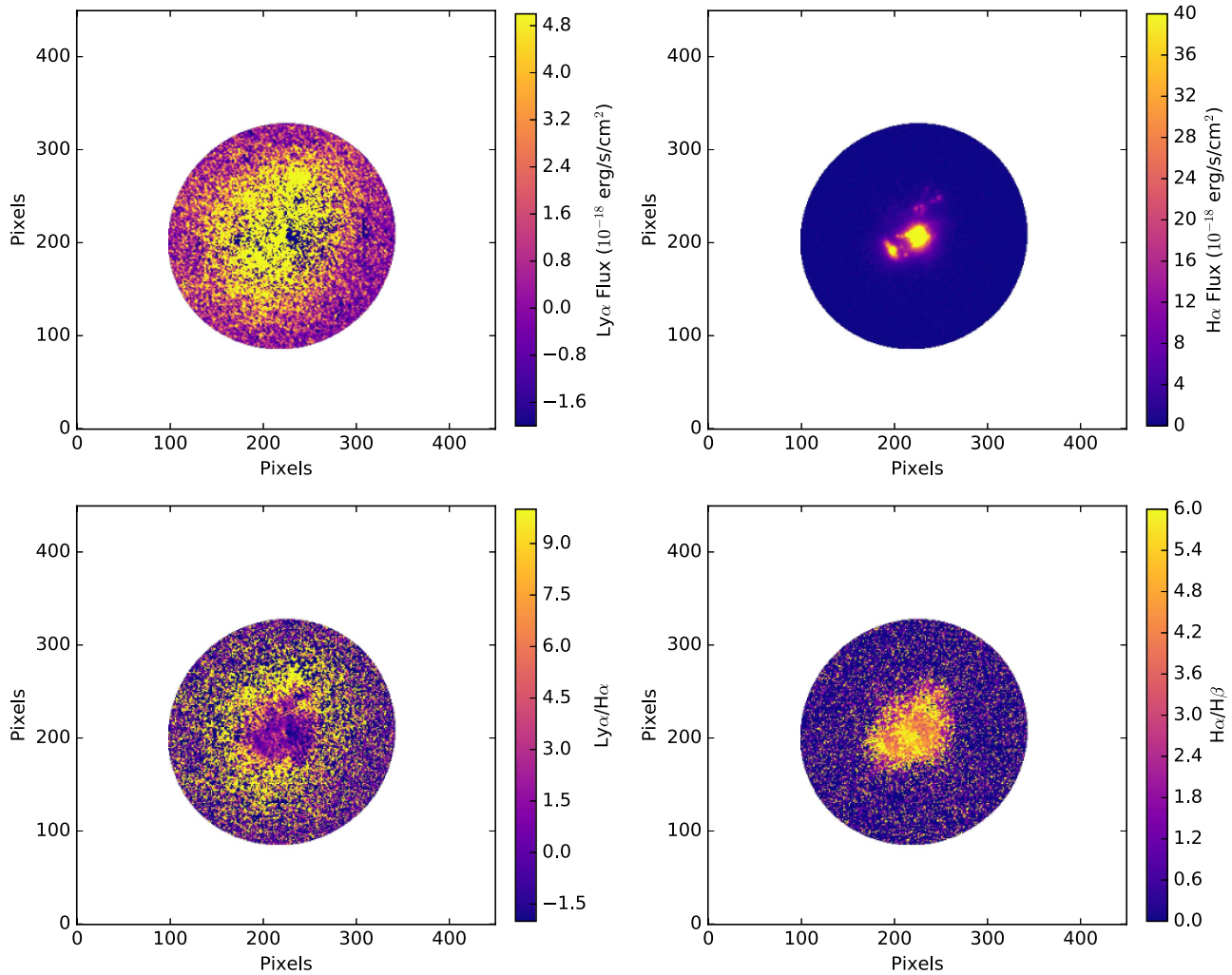
Figure 3. Images of LARS12. The calculated aperture has been applied. Top left: the Lyα emission map. Top right: the Hα emission map. Bottom left: the Lyα/Hα ratio, with an average uncertainty of 0.02. Bottom right: the Hα/Hβ ratio, with an average uncertainly of 0.005.

rather than escaping directly through holes blown through the ISM by galactic winds.

We present figures similar to Figures 6 and 7 for the other LARS galaxies in the Appendix. As might be expected from the results for LARS12, all of the galaxies that lie on or above the Cardelli model in Figure 1 (LARS03, 08, 11, and 13) show little to no cavity in the center of the galaxies. Rather than forming an annulus, the pixels corresponding to the clumpy dust model exist all the way to the center. In contrast, most of the galaxies of this study possess a scattering halo where Lyα is overly bright compared to Hα.

4. An Empirical Model for Lyα Scattering

Here, we present a model to quantify how much Lyα photons scatter in galaxies. This model is based on the observations of dust geometries present in the LARS galaxies. To model the emission of Lyα, we begin with an examination of the relative intensities of Lyα and Hα in the LARS galaxies. Deviations from the intrinsic ratio of Lyα/Hα ∼ 8.7 capture the physics of Lyα radiative transfer. At gas densities that are relevant in typical interstellar media, the opacity of the Hα line is negligible. Our goal is to quantify this difference between Hα and Lyα, and thereby probe the effect that environment and dust geometry have on Lyα scattering. There is a stark

difference between the Lyα and Hα emission shown in Figures 2 and 3, highlighting the scattering that Lyα photons undergo. By using the Hα (with Hβ to correct for reddening) images and our knowledge of the intrinsic Lyα/Hα ratio, we can calculate the intrinsic Lyα emission that should exist in comparison to what is actually observed.

4.1. Model Description

Our scattering model is based on the observed properties of the dust absorption and photon scattering discussed in Section 3.2. LARS01 shows that the pixels corresponding to a clumpy dust model congregate in an annulus around a central region within which the Lyα emission is brightest and only slightly extinguished. Meanwhile, the pixels that are overbright in Lyα compared to Hα, which is an indication of scattering back into the line of sight, form the Lyα halo. Following this, we posit a three-component galaxy model: a central region in which the Lyα photons are attenuated by only a uniform dust screen, an annular region that contains a clumpy dust geometry, and finally an outer halo region with no dust where the Lyα photons can scatter out to large distances. Of particular interest are how and how much the Lyα photons scatter in the halo region, as one of the big questions about Lyα escape is how the dust affects the escape of Lyα photons.
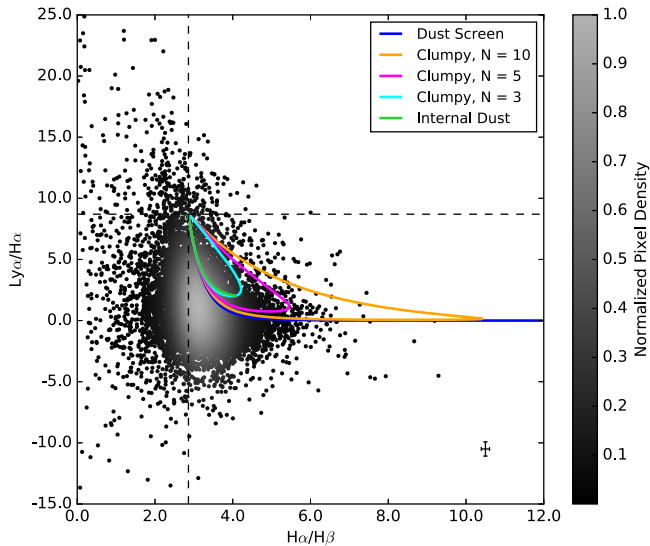
Figure 4. Lyα/Hα vs. Hα/Hβ for LARS01. The uniform dust screen model is plotted as a blue line, and three different clumpy dust models for $N = 3, 5, 10$ are shown in orange, magenta, and cyan, respectively. The smooth internal dust model is plotted with a green line. The horizontal black dashed line indicates the intrinsic ratio of Lyα/Hα ∼ 8.7, and the vertical dashed line shows Hα/Hβ = 2.86. The normalized density of points is shown in the gray scale (determined using a Gaussian kernel density estimator). The median error bar is shown in the bottom right corner.
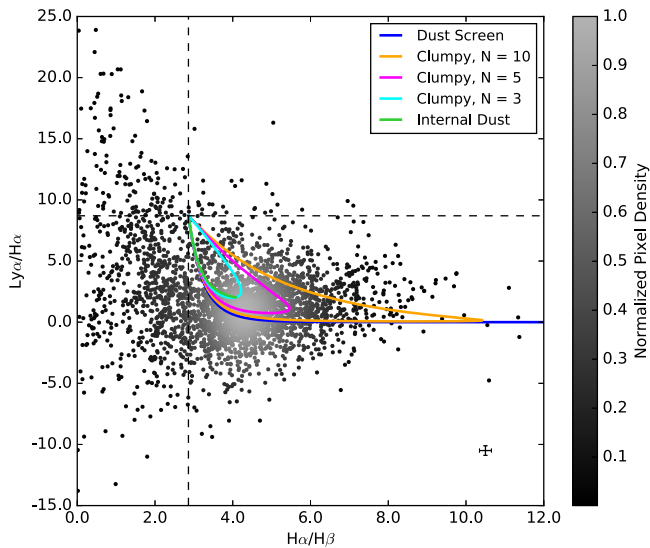
Figure 5. Same as Figure 4 but for LARS12. LARS12 is generally a redder galaxy, and many more pixels lie in the clumpy dust model regions than for LARS01.

We begin multiplying the 2D Hα emission line map by the intrinsic ratio of 8.7 to obtain an estimate of the intrinsic Lyα distribution that is unaffected by dust or scattering. We then create three separate images: one derived using a dust screen model, another using a clumpy dust model, and a third where the scattering of Lyα photons is the only physical process. After each image is created, we piece them together, using the dust screen model for the central region, the clumpy dust model in an annulus around the center, and the scattering model for the outer regions. Below, we describe the details of each segment, and how the sizes of each region are determined.

We modulate the central region Lyα emission with a simple dust screen model with

$$E(B - V) = \frac{2.5}{k_{H\beta} - k_{H\alpha}} \log_{10}\left(\frac{H\alpha/H\beta}{2.86}\right), \quad (2)$$

where $k_{H\alpha} = 2.455$ and $k_{H\beta} = 3.520$, as described by Cardelli et al. (1989). Here, the Hα/Hβ values used are drawn randomly from the Balmer decrement distribution for the galaxy being modeled and applied to each pixel in the central region. The reason we draw randomly from a distribution of Balmer decrements rather than the measured value for each pixel is because the Hβ is not always well measured, making a reliable value at each pixel impossible to determine. This extinction is then applied as

$$L_{Ly\alpha} = 8.7 \times L_{H\alpha} \times 10^{-0.4E(B-V)k_{Ly\alpha}}. \quad (3)$$

The size of the central region is a free parameter that is fit for in the model.

The annulus between the central region and the Lyα halo experiences a more complex dust component than the central region as it is assumed to contain clumpy media. This changes the effect that the dust has on the Lyα photons, resulting in a different absorption cross-section. We model this effect with Equation (1). Using the intrinsic Hα/Hβ ratio of 2.86, we calculate the number of clumps along the line of sight for each pixel in the annular region. From this set of clump values we then draw randomly to create a distribution of clumps along the line of sight in the annulus and apply the random values to all of the pixels in the region. As with the central region, the size of the annulus is determined during the model fitting. Additionally, we assume a normal distribution of τ centered around 1 with a standard deviation of 0.25. This has the effect of magnifying the absorption slightly as compared to the dust screen model applied to the central region. Other optical depth values would slightly increase or decrease the absorption in the annular clumpy dust region. The choice of this optical depth distribution was largely empirical, chosen because higher optical depths could not reproduce the surface brightness distributions from the annular region. Using a global distribution of τ centered at 1 is a simplifying assumption, but its use does not change qualitatively the overall conclusions drawn from the model outputs.

To model the Lyα halo at large radii, we "scatter" the photons by convolving the simulated Lyα (where Lyα = 8.7 × Hα) emission with a symmetric two-dimensional Gaussian kernel. The convolution operation empirically mimics the effect of scattering the Lyα from the centralized emission that is seen in the Hα maps toward larger angular distances seen in the Lyα halo. That a Gaussian two-dimensional kernel is appropriate can be understood from the radiative transfer point of view: once in the wings of the line, a Lyα photon performs a random walk (Adams 1972). An ensemble of random "walkers" in an inhomogenous medium will result in a Gaussian distribution after sufficient steps (Gronke et al. 2016, 2017). Other kernels were tested, such as a Lorentzian kernel, with similar results.

The resulting model has three input parameters: the average scattering distance of Lyα photons in the halo region, represented by the Gaussian kernel width, the isophotal size of the central region, and the isophotal size of the annulus. We parameterize the sizes of the two regions as a fraction of the aperture calculated in Section 2.
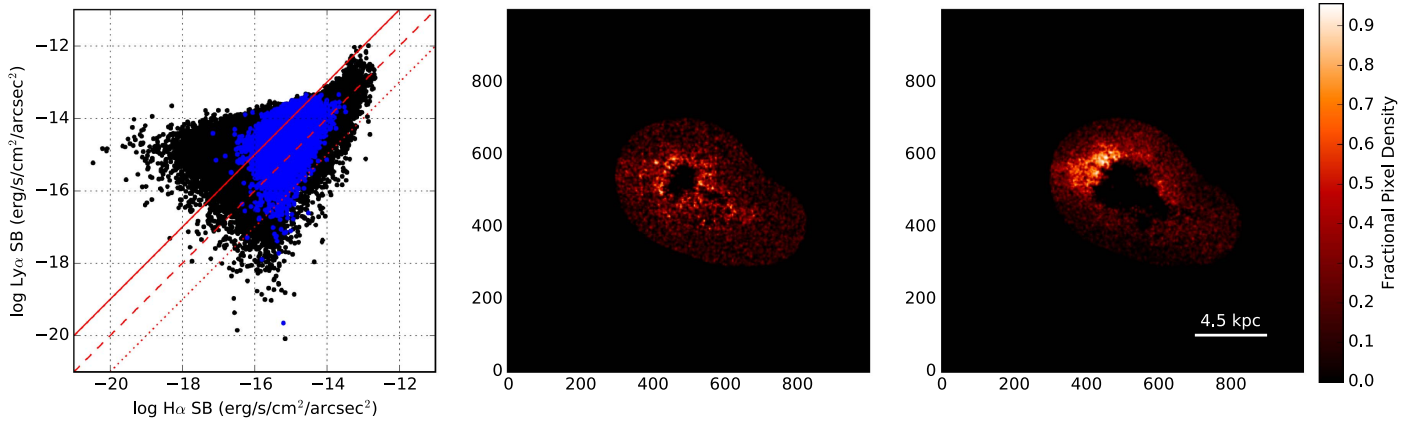
Figure 6. Left: log Lyα surface brightness vs. log Hα surface brightness for LARS01. Overplotted in blue are the pixels in the galaxy that lie above the simple dust screen model (Figure 4). Note that because the values are plotted on a logarithmic scale, only positive values are included. The solid red line indicates the intrinsic value of Lyα vs. Hα surface brightnesses under Case B recombination, and the dashed and dotted red lines show a one-to-one relation and ten times below that, respectively. Center: the blue pixels in the left panel are traced back to their origin in the Lyα image. The calculated aperture has been applied to each galaxy. The color scale of the image corresponds to how densely the pixels are packed, with the lighter colors showing a greater number of pixels in the region and the dark colors showing no pixels that correspond to the blue pixels on the left. The color scale is normalized to one. Right: the Lyα image showing only the pixels that lie above the intrinsic Lyα/Hα value denoted by the solid red line in the left panel. These are the pixels that indicate scattering of Lyα photons into the line of sight, and largely trace the diffuse Lyα emission.

To find the best-fit model for each galaxy, we use a Markov Chain Monte Carlo (MCMC) implementation called `emcee` (Foreman-Mackey et al. 2013). This technique ensures that the parameter spaces for each input are fully explored without being excessively computationally expensive. For each iteration of input parameters, we compare the simulated Lyα versus Hα surface brightness distribution to the observed surface brightness distribution to determine which set of parameters best fits the data. We do this by first creating a 2D histogram of the original Lyα versus Hα surface brightness distribution. After each iteration in the calculation, a new surface brightness distribution is created and a 2D histogram of that distribution is made. To compare the observed and modeled surface brightnesses, we test the fit by minimizing the quantity

$$\sum_{i,j=0}^{n} \frac{(\text{Observation}[i,j] - \text{Model}[i,j])}{\text{Observation}[i,j]}, \qquad (4)$$

where n is the number of bins, and (i, j) represents the bins of the 2D histogram. The output of `emcee` is the kernel width and region sizes that best match the observed surface brightness distributions.

4.2. Model Results

In Figures 8 and 9, we compare the observed Lyα versus Hα surface brightnesses to our simulated values. For LARS01, the resulting scattering kernel is $\sigma = 0.72^{+0.38}_{-0.27}$ kpc, where the errors give the 16th and 84th percentiles of the walkers from the MCMC algorithm. This kernel encodes the average scattering distance that each Lyα photon undergoes in any given galaxy. In contrast, the halo surrounding LARS12 has a Lyα photon scattering distance of $\sigma = 1.03^{+1.74}_{-0.69}$ kpc. The best-fit scattering model for all of the LARS galaxies is given in Table 2.

The right panels of Figures 8 and 9 show the models for the Lyα versus Hα surface brightnesses. Note that the pixels in the brightest Lyα region lie directly on the Case B recombination line or just below it—this is because in the central regions, only a dust screen model is applied, meaning that there is no way for

the photons to scatter to *brighter* Lyα values. The clumpy dust annulus corresponds to the region further down and to the left in the surface brightness distribution, where there is more reddening due to the clumpy nature of the dust, so Hα is dampened compared to the Lyα. The region of the figure with the overbright Lyα compared to Hα is from the Lyα halo. Note that in our model, the borders between the three zones are sharp, whereas in the data, the transitions are more gradual. For example, both Figures 8 and 9 show a distinct corner in the simulated surface brightness distributions where the annular clumpy dust butts up against the brighter Lyα pixels that are above the intrinsic Lyα/Hα line. The natural conclusion is that there is a continuum to the region edges as they bleed into each other, and/or that some radiative transfer physics is not being captured by the model. This difference is apparent in the models for both LARS01 and LARS12. For the model comparisons for all LARS galaxies, see the Appendix.

In Figures 10 and 11, we show the fractional differences between the model and the observed Lyα and Hα surface brightnesses. While the model itself is performed on individual pixels, in order to determine how well the model matches the observed distribution, we binned both the observed and modeled distributions, and compared how many pixels exist in each bin. We chose a large number of bins (60×60) to be able to compare on a fairly fine scale, while still maintaining enough points in each bin. The differences were then calculated by finding the observed minus predicted differences in each bin. A positive difference (purple) indicates that there are more points in the observed bin than the model bin. Negative differences (yellow) occur where there are more points in the model bin than the observed. From the figures, it is apparent that our model matches the surface brightness distribution for LARS01 very well. For LARS12, the differences are more stark, with the model distributing points that should be in the Lyα halo (shown in yellow in Figure 11) to the area of the surface brightness distribution that corresponds to the clumpy annulus (shown in purple in the same figure.)

The characteristic scattering distances for the LARS galaxies range from a fraction of a kiloparsec to several kiloparsecs, and
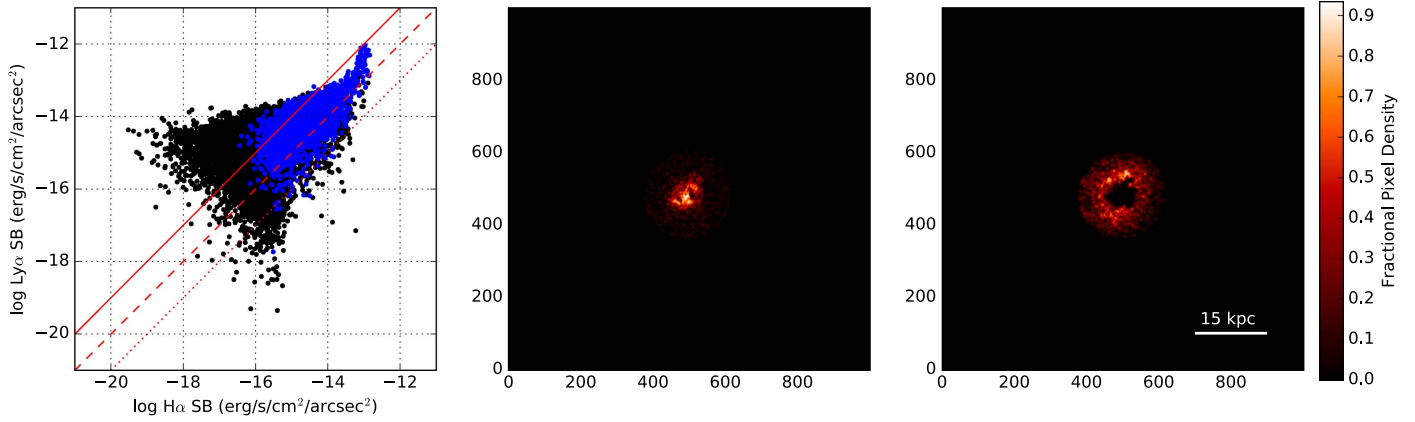
Figure 7. Same as Figure 6 but for LARS12. LARS12 shows evidence of clumpy dust almost all the way to the center of the galaxy, save for a small region (just several pixels wide) at its center.

are shown in Figure 12. We discuss the implications of these results in the following section.

5. Discussion

The Lyα scattering model presented here works very well for galaxies that exhibit the dust geometry for which it was designed—namely, those galaxies that have a central region with a non-clumpy dust distribution at the center, an annulus of clumpy dust, and a Lyα halo generated by scattering of photons. The model has difficulty reproducing the pixel distributions that indicate clumpy dust all the way to the center of the galaxies, which would result in little or no central region at all. Table 2 shows central region sizes that do not correspond well with what is observed. LARS12, for example, shows a small cleared central region a few pixels wide (0.4 kpc), while the model indicates a central region of $1.23^{+2.46}_{-1.06}$ kpc. As can be inferred from the error bars, this value is not very well-determined.

We note also that this model works best on the galaxies with symmetric reddening distributions. For example, the Balmer decrement distribution of LARS03 is skewed to the red and has a median value of $H\alpha/H\beta = 5.78$. Our best-fit model for LARS03 gives a Lyα halo scattering distance of $\sigma = 0.351$ kpc, but the resulting Lyα versus Hα surface brightness distribution deviates rather significantly from the observed data. LARS12 is another red galaxy, with a median Balmer decrement value of $H\alpha/H\beta = 4.35$. Our difficulty in matching its surface brightness distribution can be seen in the right panel of Figure 9, where Lyα is in places underpredicted relative to Hα. This may be due in part to the fact that we determine the reddening by drawing from a distribution, rather than using the actual $H\alpha/H\beta$ values for each pixel. If the galaxy is skewed very red, the Lyα pixels from the more central regions are pulled downwards in the surface brightness distribution. However, for galaxies with reddening distributions that are more Gaussian and with lower median $H\alpha/H\beta$ values, our model does quite well predicting the shape of the observed surface brightness distributions.

Another issue is that some galaxies show what appears to be two populations in the simulated surface brightness distribution (e.g., see Figure 9). This is an artifact of separating the galaxies into three discrete regions. In some galaxies, such as LARS01, the resulting distribution of pixels centers in the same place as the observations (see Figure 8) and the result is a good fit. But

for other galaxies, the pixels do not get distributed as evenly, leaving some evidence of the different dust models imprinted on the Lyα versus Hα surface brightness. For the same reason, the pixel density is occasionally too high along the intrinsic Lyα versus Hα line, as the best-fitting dust model does not distribute the pixels evenly.

The part of the model that best reproduces the surface brightness distributions is that associated with the Lyα halo. The Gaussian smoothing kernel does well at mimicking how the Lyα photons scatter in the halo. This result can be seen in Figures 8 and 9 as well as the similar figures for the other LARS galaxies in the Appendix. Therefore, while the model may have difficulty reproducing some dust geometries, the results of the characteristic scattering distance of Lyα photons in the halo are robust. The one exception to this is LARS06 (see Figure 30), which, as a net Lyα absorber, has very little Lyα halo.

As shown in Figure 13, the scattering distances scale linearly with the sizes of the Lyα halo for each galaxy, with a Spearman (1904) correlation coefficient of $\rho = 0.62$ and a probability of a correlation arising by chance of 1.9%. Here, the distance of the outer edge of the annulus was determined by the fitting algorithm, and since the radius of the overall aperture was fixed, the size of the outer halo region follows directly. The relationship between the characteristic scattering distance and the size of the halo is intuitive, as a galaxy with a longer characteristic Lyα photon scattering distance will experience more Lyα escape, resulting in a larger halo.

The amount of Lyα scattering should be strongly related to the density of the neutral scattering medium in a galaxy. We explored this relationship using data for the LARS galaxies from the Very Large Array (VLA; Pardy et al. 2014). At present, data are published for only five galaxies in the sample: LARS02, LARS03, LARS04, LARS08, and LARS09. We note that there is a possible positive correlation between the scattering distance and the H I column density as shown in Figure 14. However, this correlation is pinned only by LARS04, for which the scattering distance has large error bars. More extensive H I observations will be able to determine whether or not this correlation actually exists.

The fact that the size of the Lyα halo correlates with the scattering distance means that the halo is produced mainly by scattering of H I within the galaxy. Therefore, no other phenomena in addition to scattering is required to explain the halos. This conclusion was also reached work based on
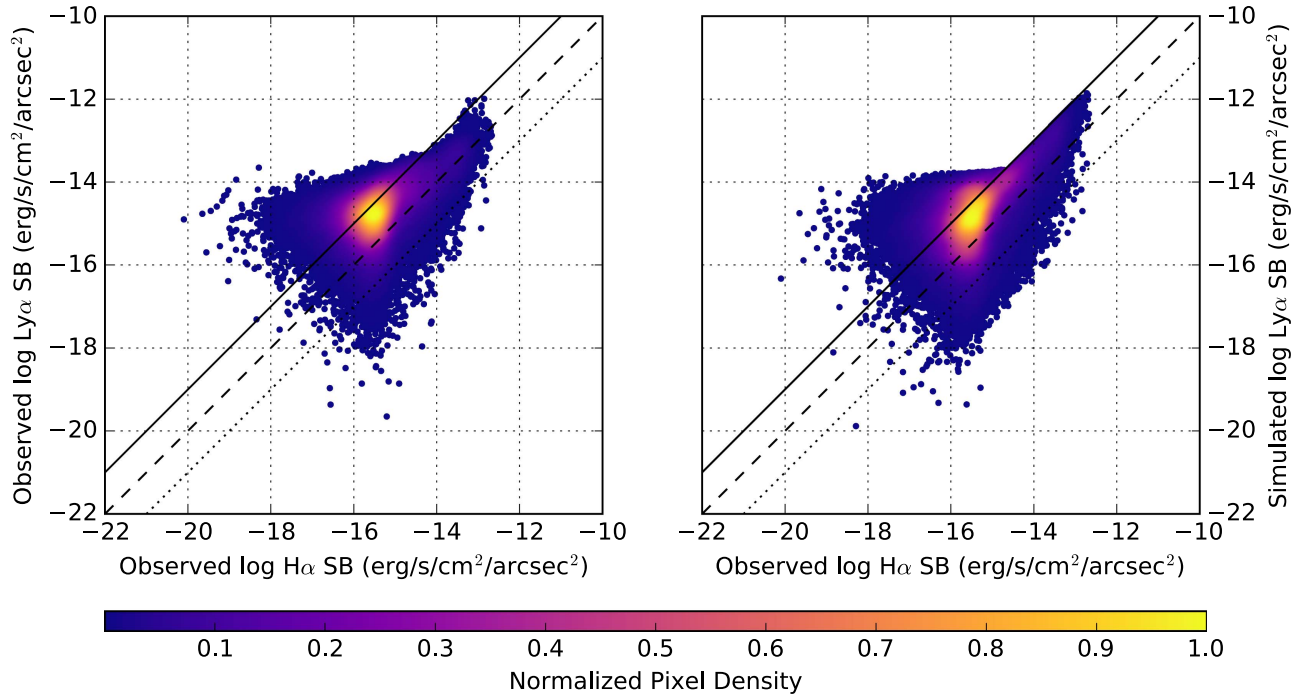
Figure 8. Surface brightness plots for LARS01. Shown in the left panel is the observed Lyα surface brightness vs. Hα surface brightness. Note that because the values are plotted on a logarithmic scale, only positive measurements are included. The solid black line denotes the Case B recombination value, while the dashed line represents a one-to-one ratio of Lyα and Hα emission and the dotted line a dex below that. The right panel shows the same plot but for the simulated Lyα surface brightness from the model vs. Hα surface brightness. The normalized density of points is shown in the color scale (determined using a Gaussian kernel density estimator), and the density values shown in the color bar.
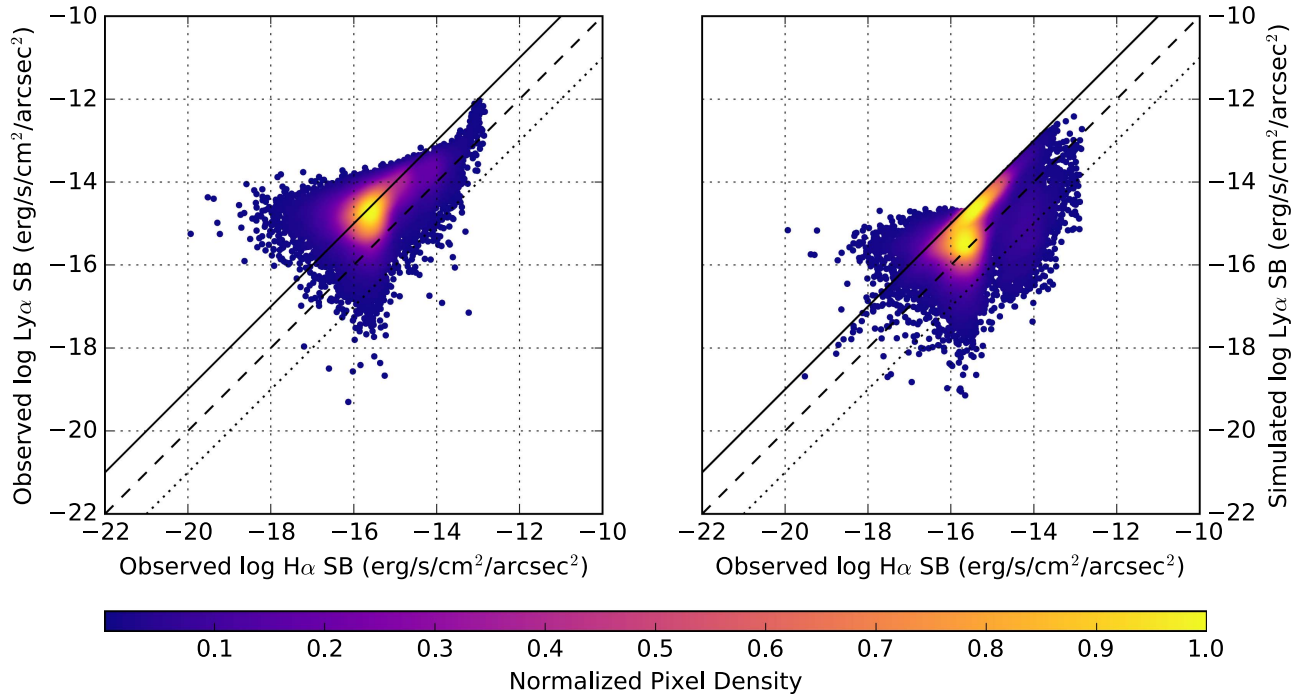
Figure 9. Same as Figure 8, but for LARS12.

spectroscopic data of $2 < z < 4$ Lyα emitters in the VIMOS Ultra Deep Survey (VUDS; Guaita et al. 2017). Relating the characteristic scattering distance with other physical parameters that are linked to the H I content (e.g., galaxy mass), would indicate that the extent of the Lyα emission depends on galaxy physical properties. This would be further proof that Lyα

photons are generated inside the galaxy and are simply scattered by the neutral hydrogen.

Figure 15 shows that there is a tentative inverse correlation between the Lyα scattering distance and the average reddening values of the LARS galaxies. The Spearman correlation coefficient for this relationship is $\rho = -0.49$ with a probability
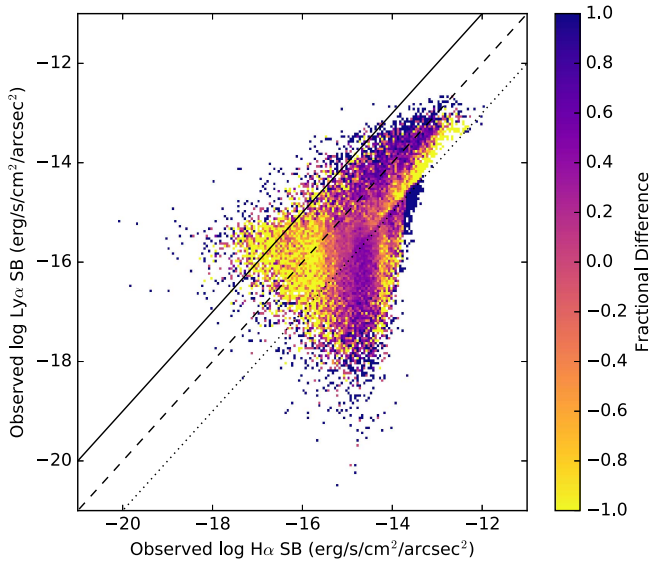
Figure 10. Fractional difference between the model and observed surface brightnesses for LARS01. The data have been binned and a positive difference (purple) indicates that there are more points in the observed bin than the model bin. Negative differences (yellow) occur where there are more points in the model bin than the observed data.
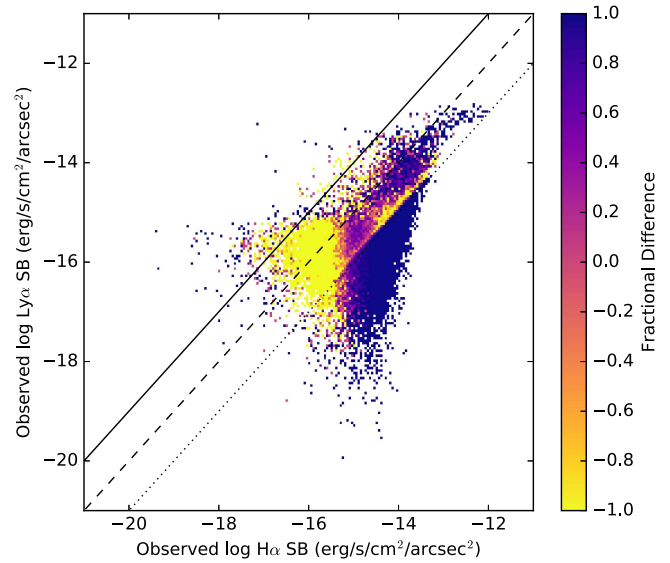
Figure 11. Same as Figure 10, but for LARS12.

Table 2
LARS Scattering Properties

LARS ID	Halo Scattering Distance (kpc)	Central Region Radius (kpc)	Annular Region Radius (kpc)
01	$0.72^{+0.38}_{-0.27}$	$0.36^{+1.35}_{-0.26}$	$2.28^{+0.16}_{-0.26}$
02	$0.36^{+0.04}_{-0.034}$	$1.52^{+0.59}_{-1.3}$	$3.50^{+0.49}_{-1.30}$
03	$0.35^{+0.05}_{-0.05}$	$3.08^{+0.31}_{-0.24}$	$3.71^{+0.36}_{-0.24}$
04	$0.70^{+0.54}_{-0.42}$	$2.17^{+0.14}_{-0.54}$	$2.92^{+2.63}_{-0.54}$
05	$0.40^{+0.08}_{-0.09}$	$1.59^{+0.46}_{-0.32}$	$2.67^{+0.58}_{-0.32}$
06	$0.41^{+0.06}_{-0.09}$	$1.94^{+0.73}_{-1.07}$	$4.39^{+0.58}_{-1.07}$
07	$0.37^{+0.14}_{-0.26}$	$1.43^{+0.32}_{-0.33}$	$2.22^{+0.47}_{-0.33}$
08	$0.44^{+0.07}_{-0.08}$	$2.71^{+1.09}_{-1.46}$	$5.58^{+1.75}_{-1.46}$
09	$0.56^{+0.11}_{-0.11}$	$0.40^{+0.13}_{-0.68}$	$7.18^{+1.55}_{-0.68}$
10	$0.52^{+0.08}_{-0.06}$	$1.35^{+0.23}_{-0.11}$	$2.30^{+0.27}_{-0.11}$
11	$1.56^{+0.03}_{-0.49}$	$6.41^{+0.50}_{-1.51}$	$6.92^{+0.21}_{-1.51}$
12	$1.03^{+1.74}_{-0.69}$	$1.23^{+2.46}_{-1.06}$	$4.77^{+1.04}_{-1.06}$
13	$2.24^{+0.18}_{-0.29}$	$3.29^{+0.52}_{-0.33}$	$6.62^{+0.31}_{-0.33}$
14	$1.68^{+2.83}_{-1.13}$	$1.96^{+3.91}_{-1.68}$	$7.58^{+1.65}_{-1.68}$

Figure 12. Distribution of the characteristic scattering distances resulting from the model. A majority of the galaxies have a scattering distance of one kiloparsec or less.

of a correlation arising by chance of 7.8%. This behavior suggests that Lyα photons do not scatter as far in galaxies with higher dust content. This is consistent with studies that show that the Lyα escape fraction decreases with dust content (Hayes et al. 2013; Atek et al. 2014).

For our scattering model, we assumed certain dust geometries based on the pixel-by-pixel distribution for each galaxy. Because LARS galaxies are bright, with vigorous star formation, one might wonder whether our results can be extrapolated to the general population of Lyα emitting galaxies. For example, the dust distribution in LBGs is best represented with a clumpy shell configuration (e.g., Vijh et al. 2003). That this same geometry of a clumpy dust annulus is found in a sample of LBG analogs at low redshift indicates that the dust behaviors evidenced by the LARS galaxies can be useful for determining higher-redshift galaxy properties (e.g., Lyα escape fraction, UV output, etc.).

The results of this scattering model indicate that some specific geometries would be useful to study in full 3D radiative transfer models, such as the 3D Monte Carlo code MCLyα of Verhamme et al. (2006, 2008). Simulations that use spherically symmetric shells of neutral gas that scatter photons to model Lyα radiative transfer have been very effective at reproducing observed Lyα spectra (in some cases even better than multiphase geometries; Gronke et al. 2015). However, Gronke et al. (2016) showed that using clumpy geometries of neutral gas with a large number of clumps along the line of sight was the best way to model the observed Lyα spectra. The observation-based model we have presented marries more complicated gas and dust geometries with the shell model, and will provide new avenues to pursue in 3D radiative transfer models.
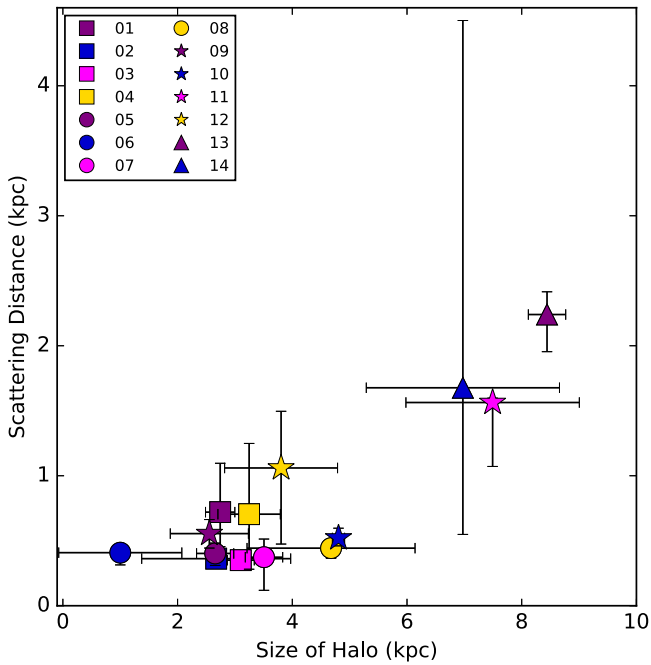
Figure 13. Characteristic scattering distances of the LARS galaxies vs. the sizes of the Lyα halos. The Lyα halo size corresponds to the size of the outer galaxy regions as determined by the MCMC fitting algorithm. The Spearman's correlation coefficient is $\rho = 0.62$ with a probability of a correlation arising by chance of $p = 0.019$. The errors give the 16th and 84th percentiles of the distribution of the walkers from the MCMC algorithm that determined scattering distance.
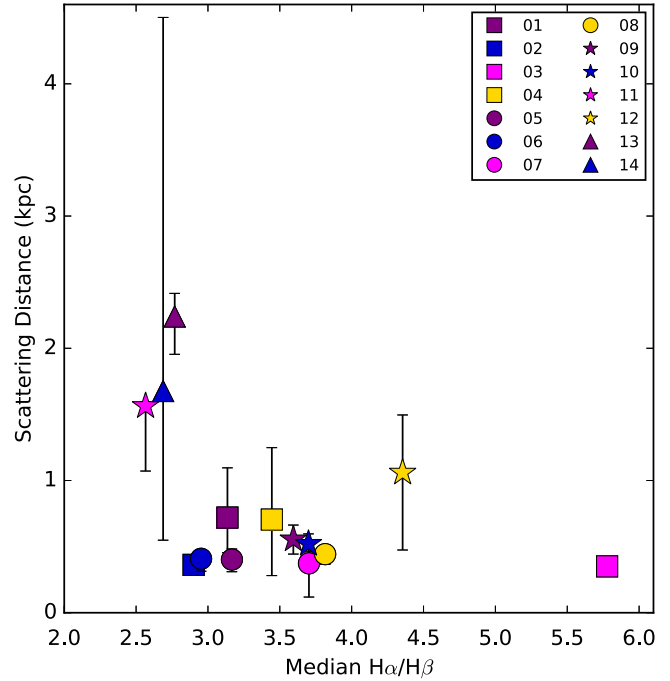
Figure 15. Characteristic scattering distance vs. the global Balmer decrement of the LARS galaxies. The Spearman correlation coefficient is $\rho = -0.49$ with a probability of a correlation arising by chance of $p = 0.078$. The errors in the scattering distance represent the 16th and 84th percentiles of the distribution of the walkers from the MCMC algorithm that determined scattering distance.
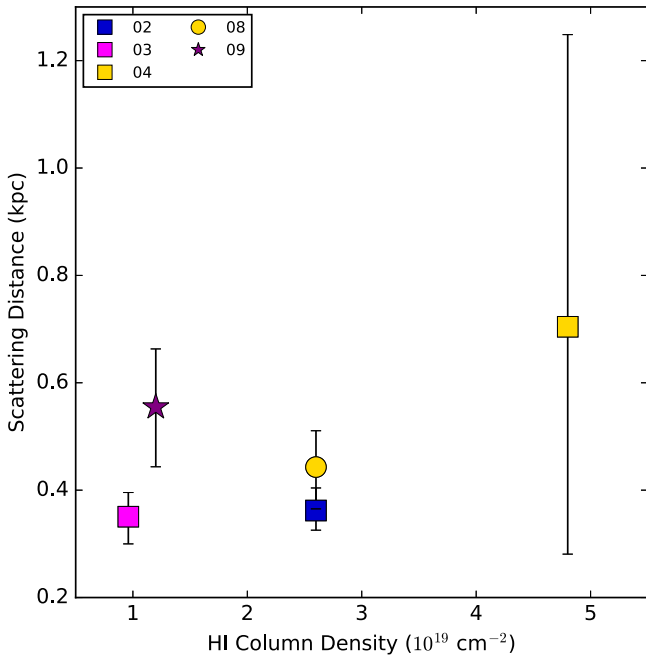
Figure 14. Characteristic scattering distance vs. the H I column density for the LARS galaxies for which these data exist (Pardy et al. 2014). The Spearman correlation coefficient is $\rho = 0.67$ with a probability of a correlation arising by chance of $p = 0.22$. The errors in the scattering distance represent the 16th and 84th percentiles of the distribution of the walkers from the MCMC algorithm that determined scattering distance.

6. Summary and Conclusions

We have presented a study of the dust geometry of the 14 LARS galaxies, and how it affects Lyα escape from galaxies. Informed by this dust characterization, we have also developed a modeling technique to characterize how far, on average, Lyα photons scatter into the outer halo before escaping.

The LARS galaxies provide a unique data set with which to use pixel-by-pixel photometry to probe the galaxies' dust geometry down scales of ∼40 parsecs. This has allowed us to move from looking only at the global dust properties of the galaxies to understanding which galaxy regions are affecting the global properties the most.

Using LARS01 and LARS12 as examples of galaxies with quite different dust distributions, we probed the properties of each galaxy, including which regions correspond to a clumpy ISM, and which regions contain the most scattering. We found that for LARS01, with a global Lyα/Hα value that places the galaxy in a region not well described by a clumpy medium, there are three distinct regions that determine the way in which Lyα escapes. At the center of the galaxy, Lyα escapes at or slightly below the intrinsic Lyα/Hα ratio of 8.7, implying little dust or neutral hydrogen along the line of sight. A clumpy medium surrounds the center in an annulus of pixels that are well described with a large number of small dust clouds. Finally, there exists a Lyα halo from which the overluminous (Lyα/Hα > 8.7) Lyα photons scatter out to great distances before leaving the galaxy.

In contrast, the sizes of the regions of LARS12 are significantly different than for LARS01. For this galaxy, the clumpy ISM extends almost to the very center of the galaxy, with only a small central region where the dust screen model is applicable. Otherwise, LARS12 has the typical Lyα halo seen in many of the LARS galaxies.

Based upon these findings, we developed a model to quantify what effect these different dust regions have on Lyα escape. Our three-parameter model uses an MCMC algorithm to find the average scattering distance that Lyα undergoes in the halo of the galaxies, as well as the sizes of the areas with smooth and clumpy

dust geometries. The resulting halo scattering distances correlate with the Lyα halo sizes and are slightly inversely correlated with the median Balmer decrement of the galaxies.

Observations of the H I in the remaining LARS galaxies (PI: Cannon; ID VLA/17A-240) will reveal whether or not there is a correlation between the H I column density and the modeled scattering distances. Additionally, with an angular resolution of ∼6″, the VLA observations will be capable of determining the H I morphologies, which will allow for a more thorough exploration of how the Lyα scattering is affected by the presence of neutral hydrogen. Other future work will involve expanding our modeling algorithm to the full extended LARS (eLARS; PI: Östlin; ID 13483) sample, which comprises a further 28 nearby Lyα emitters with more disk-like morphologies and lower Hα equivalent width cuts. The applicability of this scattering model to a broader sample of galaxies will determine how robust these initial results are.

Appendix
Lyα and Hα Emission Maps and Scattering Models

We present here the Lyα and Hα emission maps as well as the corresponding Lyα/Hα and Hα/Hβ ratios for the LARS galaxies, with their apertures applied. Additionally, we include the Hα versus Lyα surface brightness distributions and trace the pixels corresponding to clumpy dust or overbright Lyα to their origins within each galaxy. Finally, we show the observed Lyα versus Hα surface brightness distributions and compare them to the empirical Lyα scattering model results. All of these relationships are show in Figures 16–51.
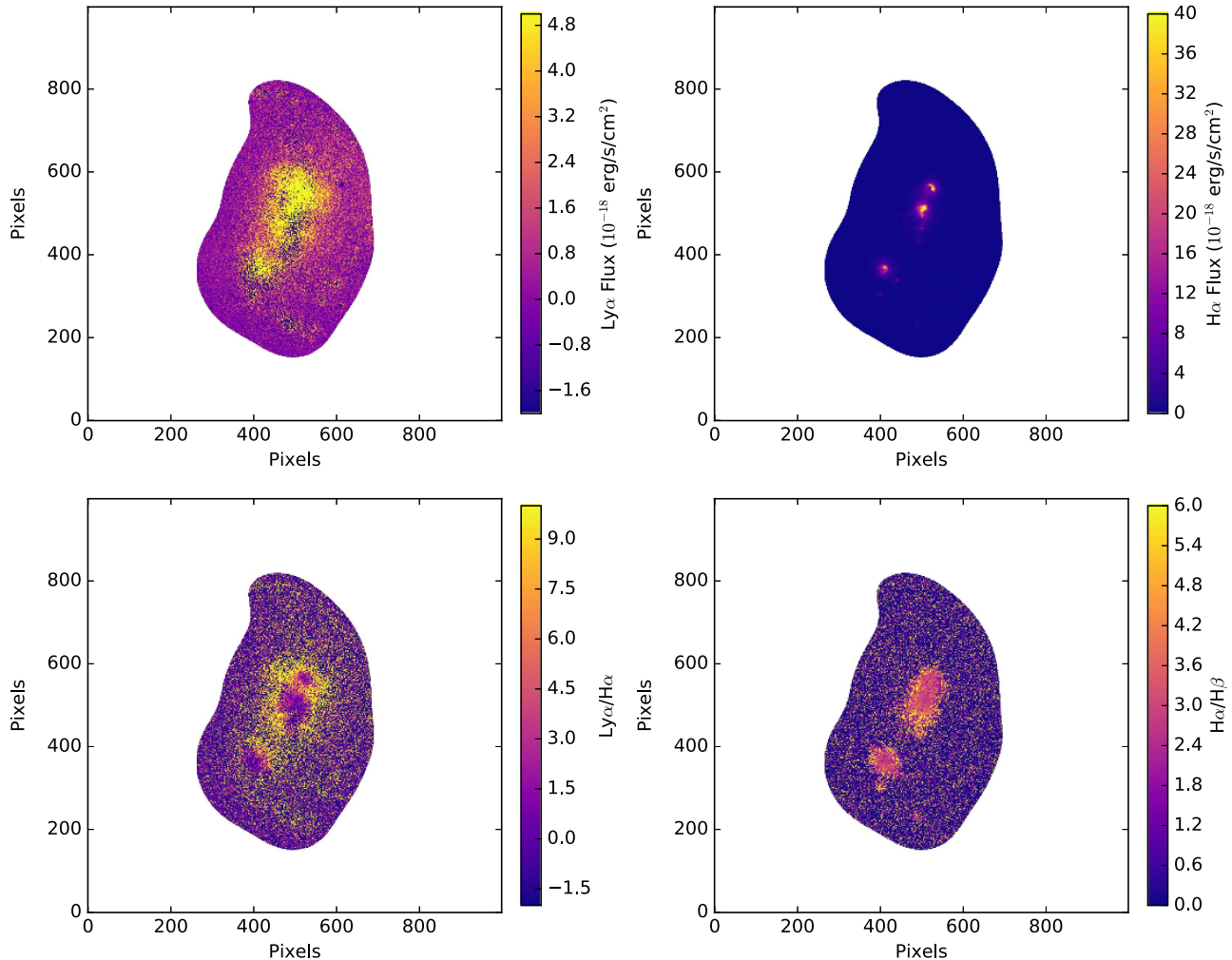
Figure 16. Images of LARS02. The calculated aperture has been applied. Top left: the Lyα emission map. Top right: the Hα emission map. Bottom left: the Lyα/Hα ratio, with an average uncertainty of 0.01. Bottom right: the Hα/Hβ ratio, with an average uncertainty of 0.001.
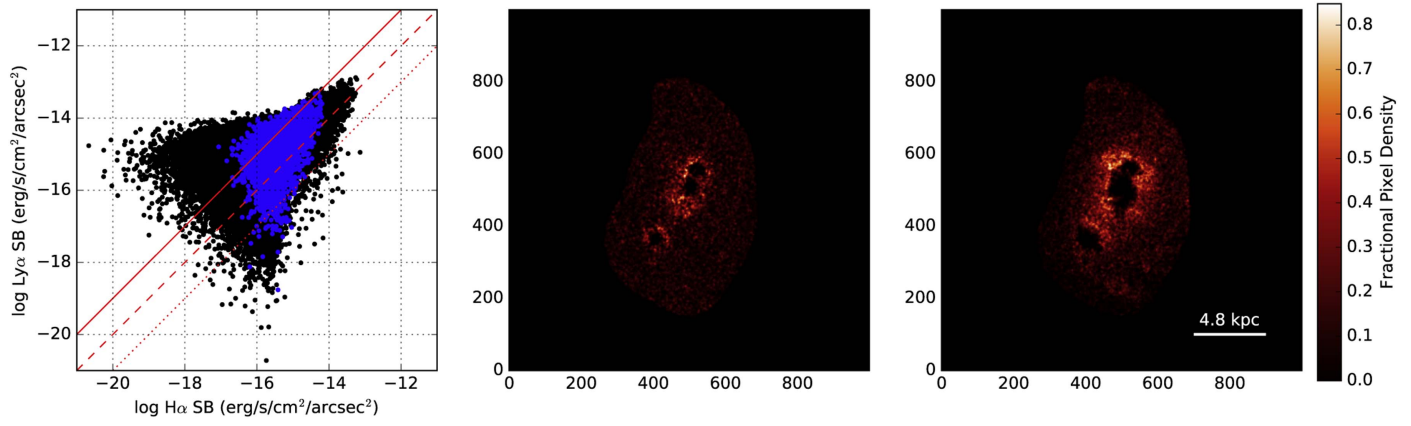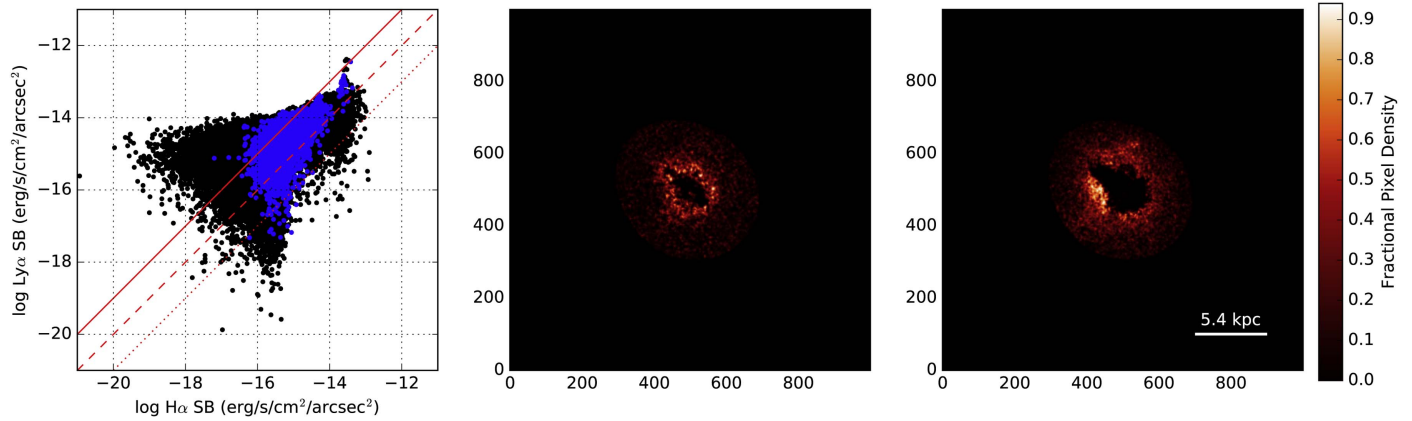
Figure 17. Same as Figure 6, but for LARS02.
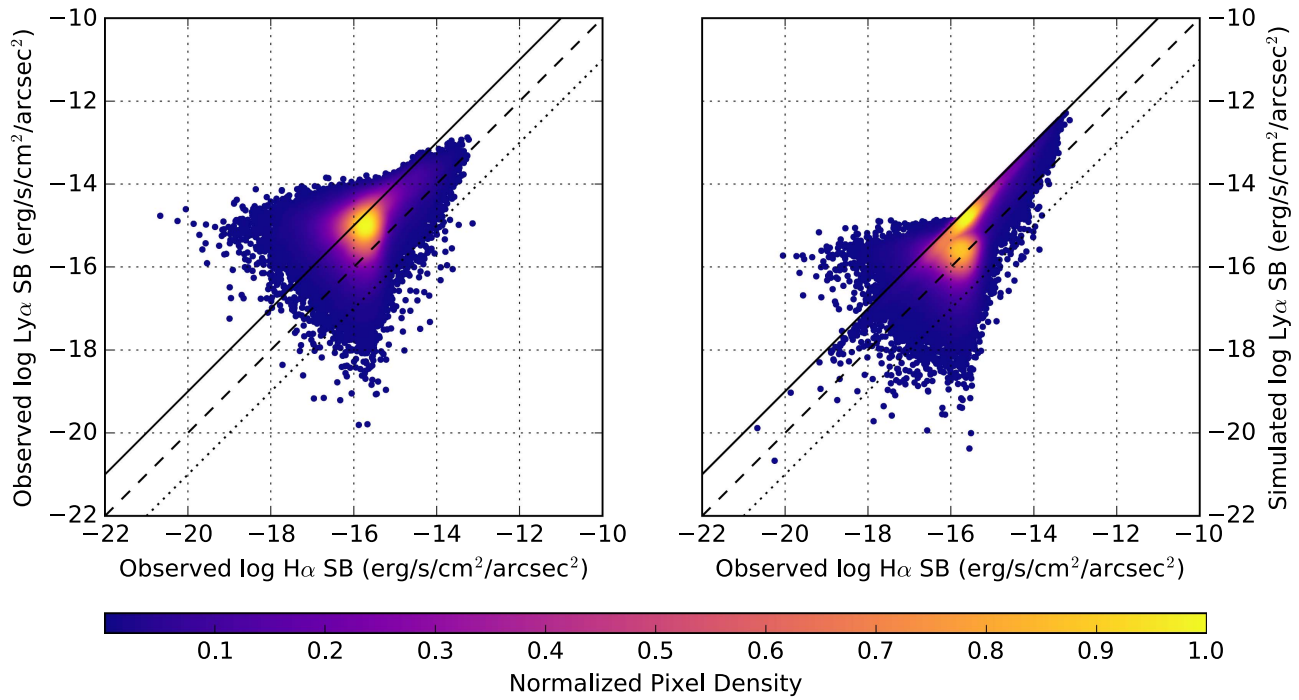
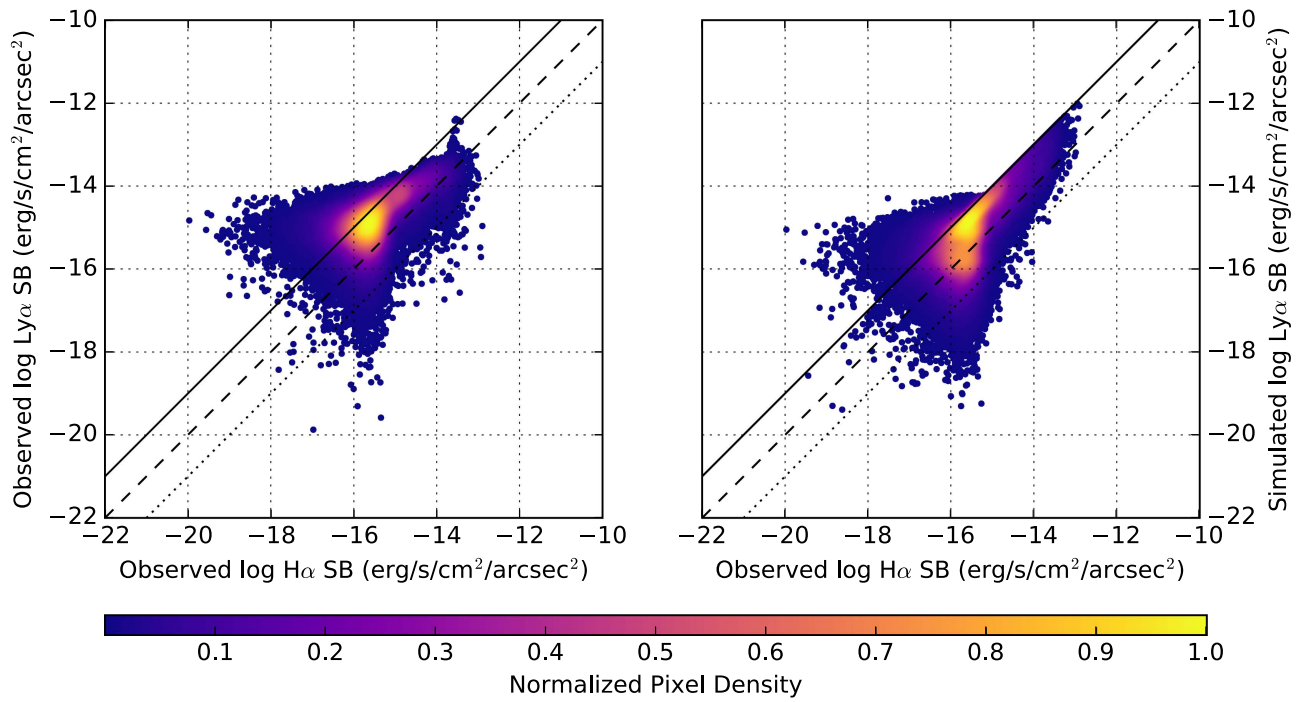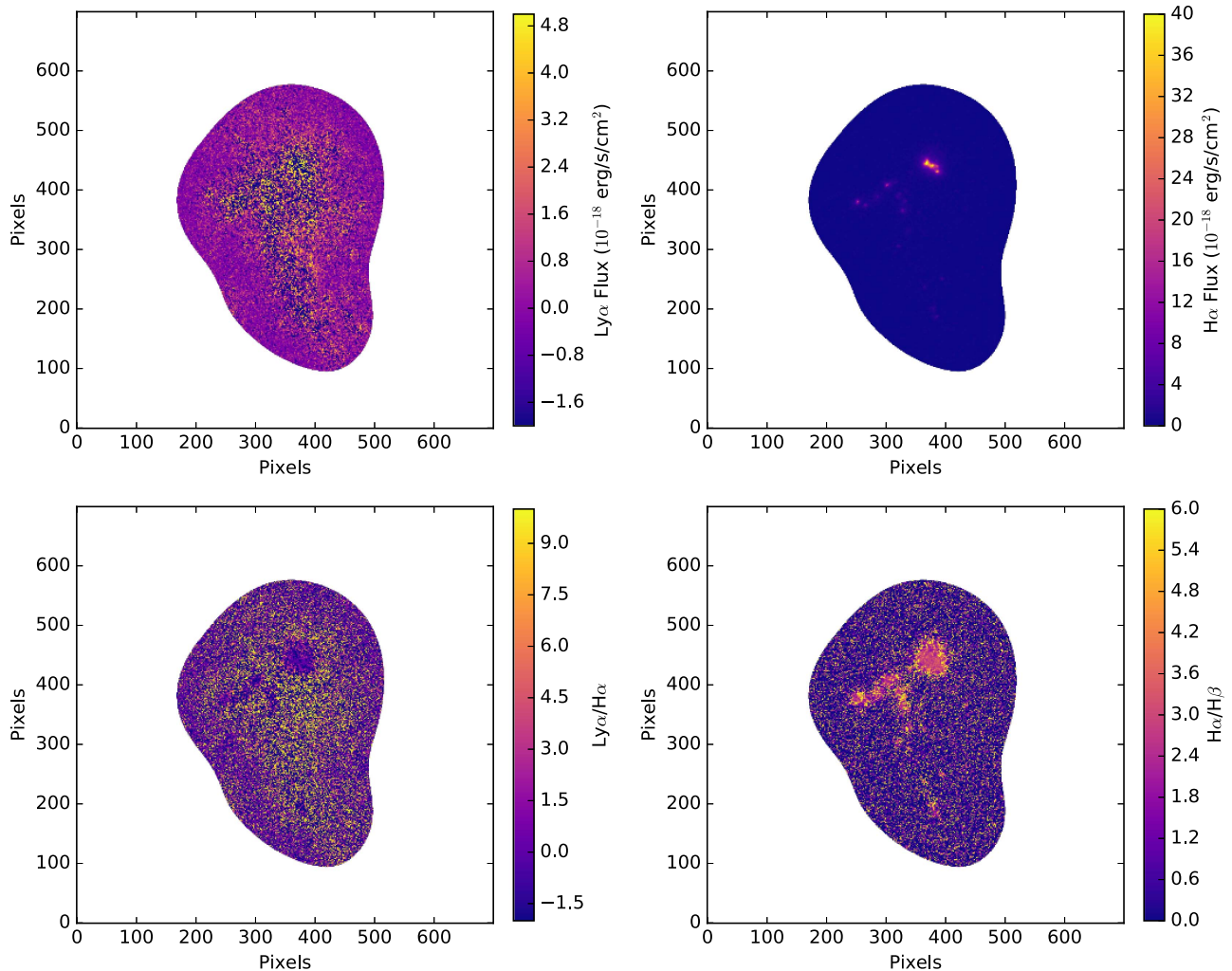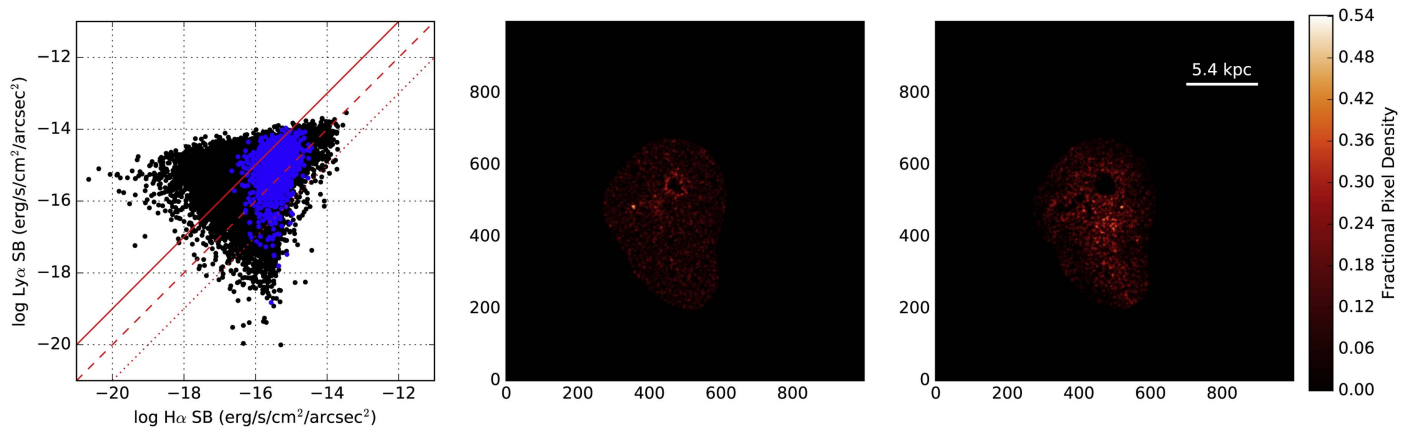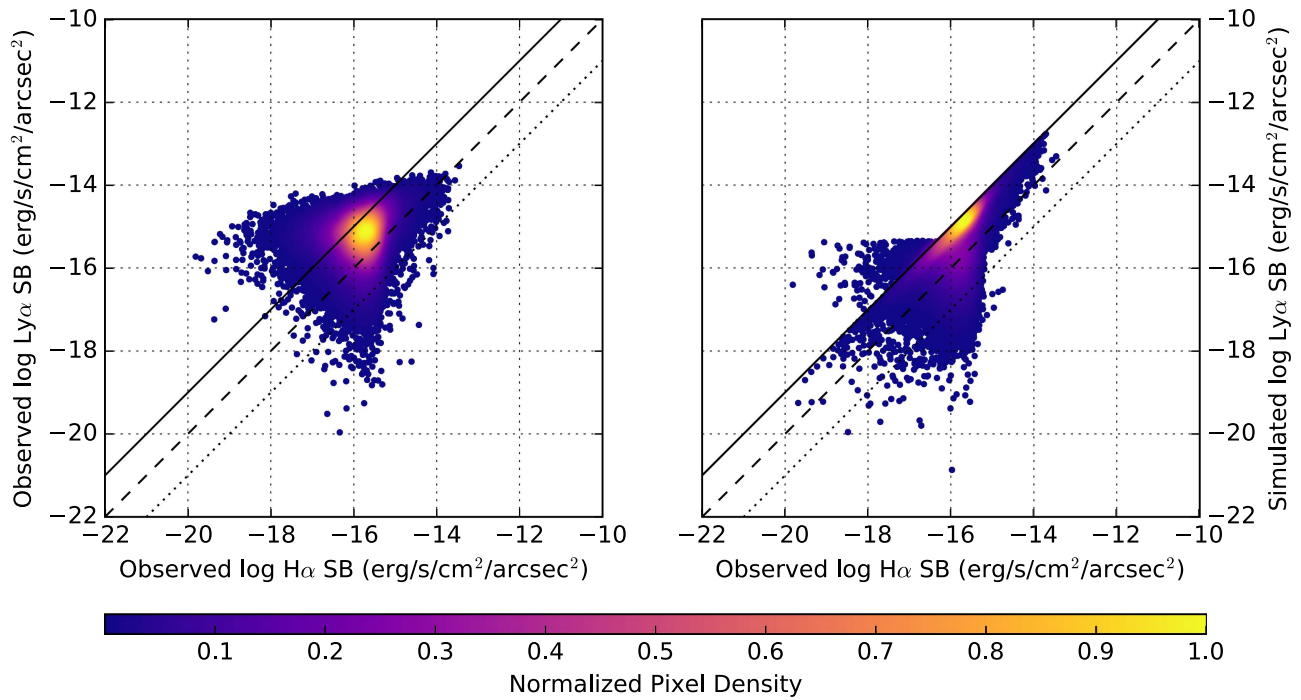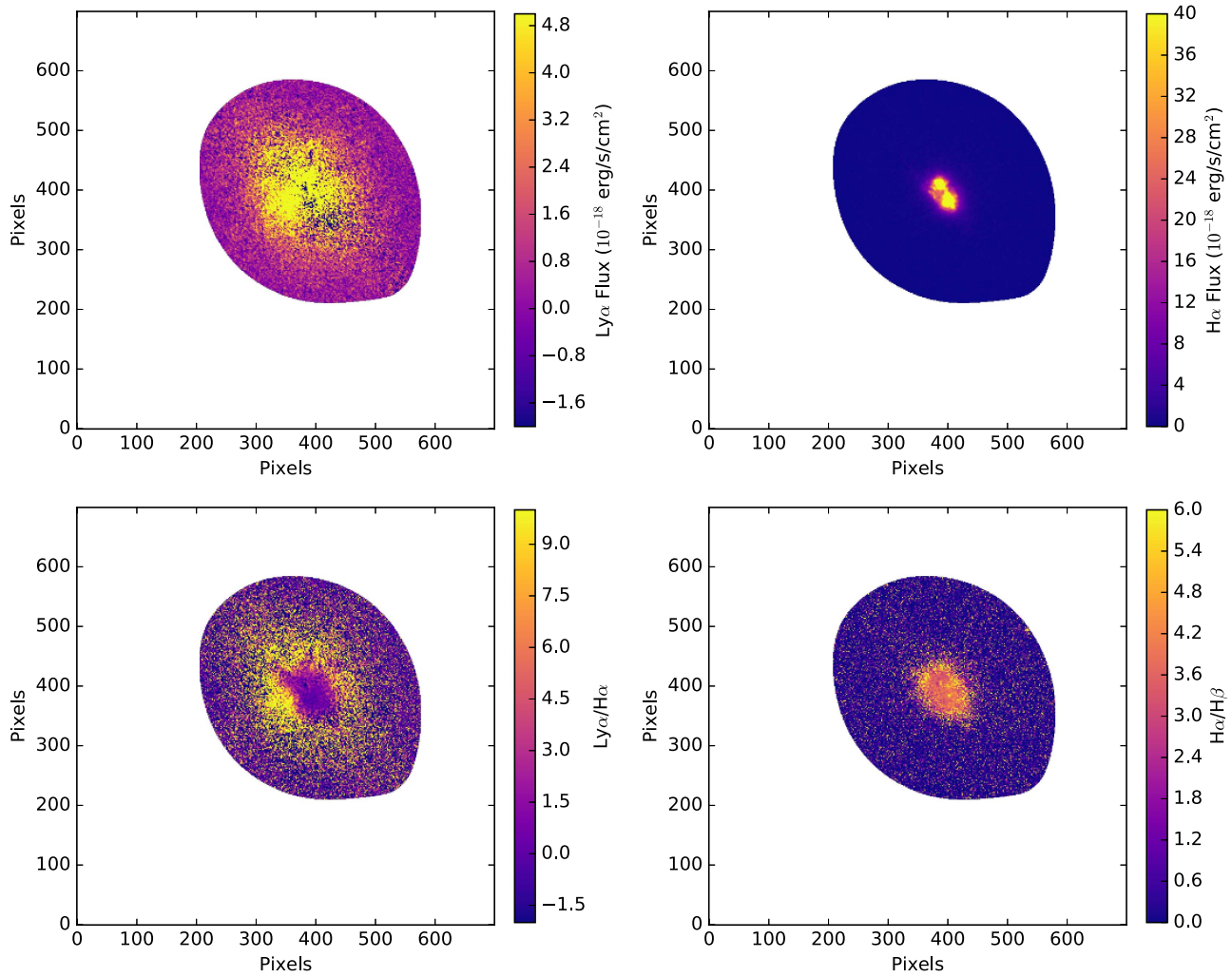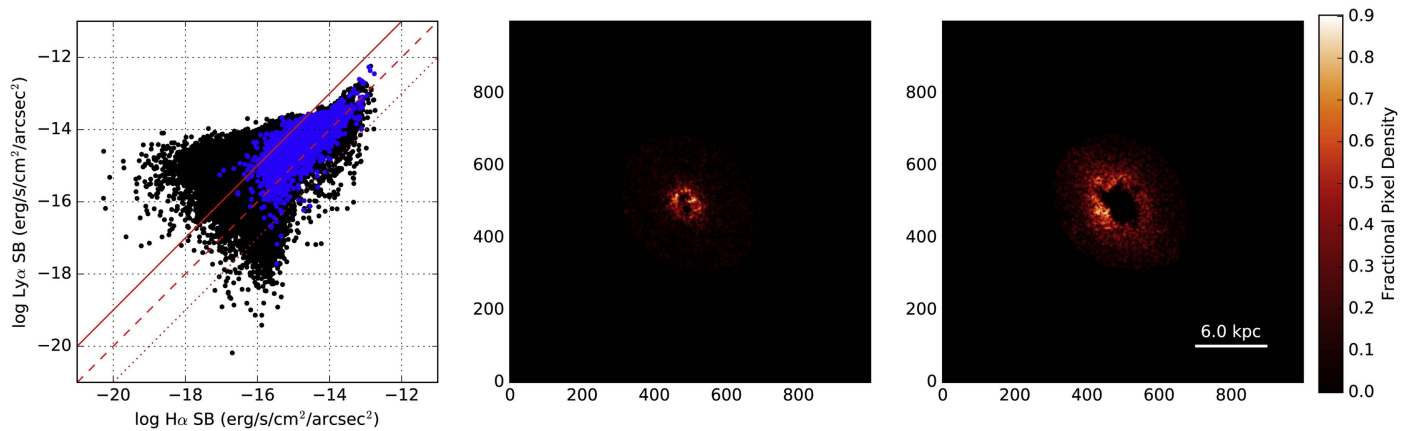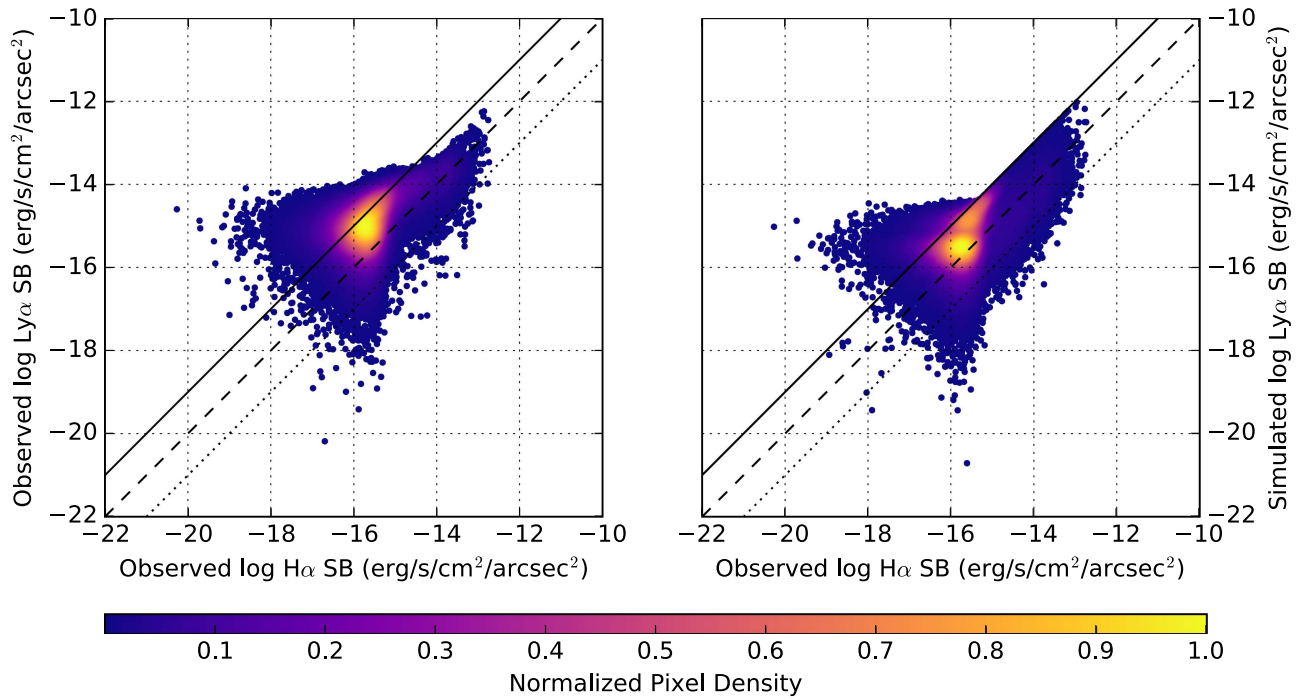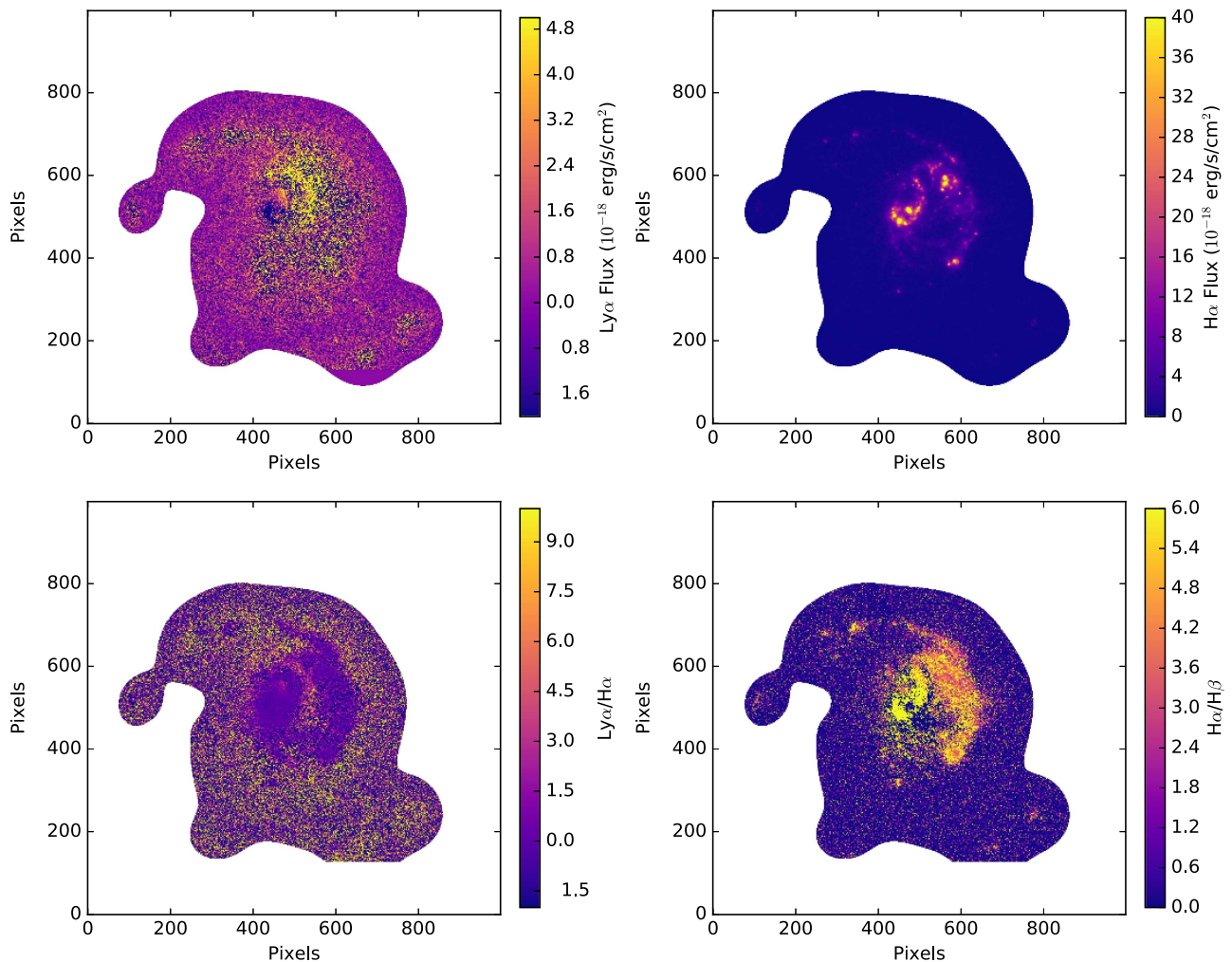**Figure 18.** Same as Figure 8, but for LARS02.
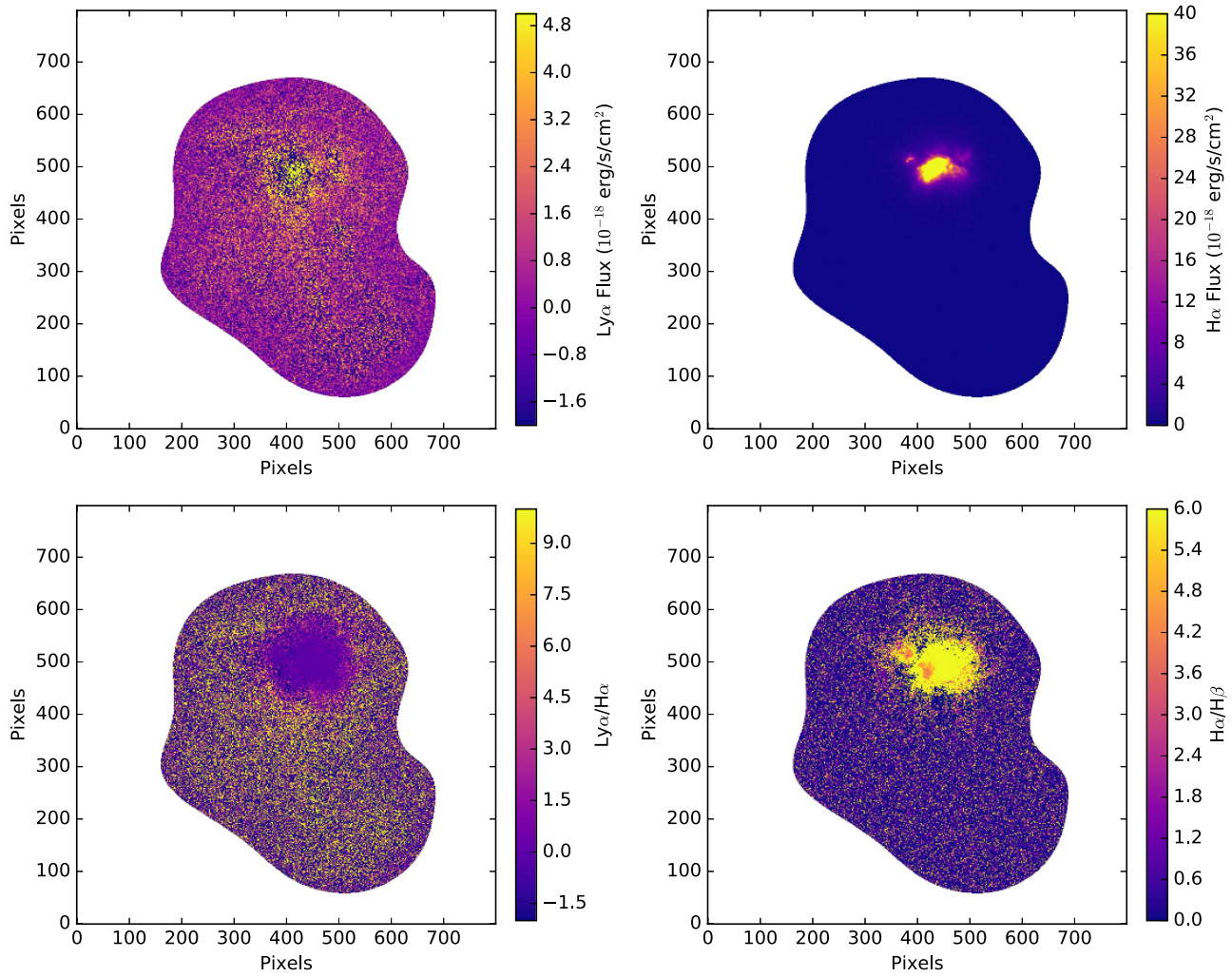
Figure 19. Images of LARS03. The calculated aperture has been applied. Top left: the Lyα emission map. Top right: the Hα emission map. Bottom left: the Lyα/Hα ratio, with an average uncertainty of 0.003. Bottom right: the Hα/Hβ ratio, with an average uncertainty of 0.009.
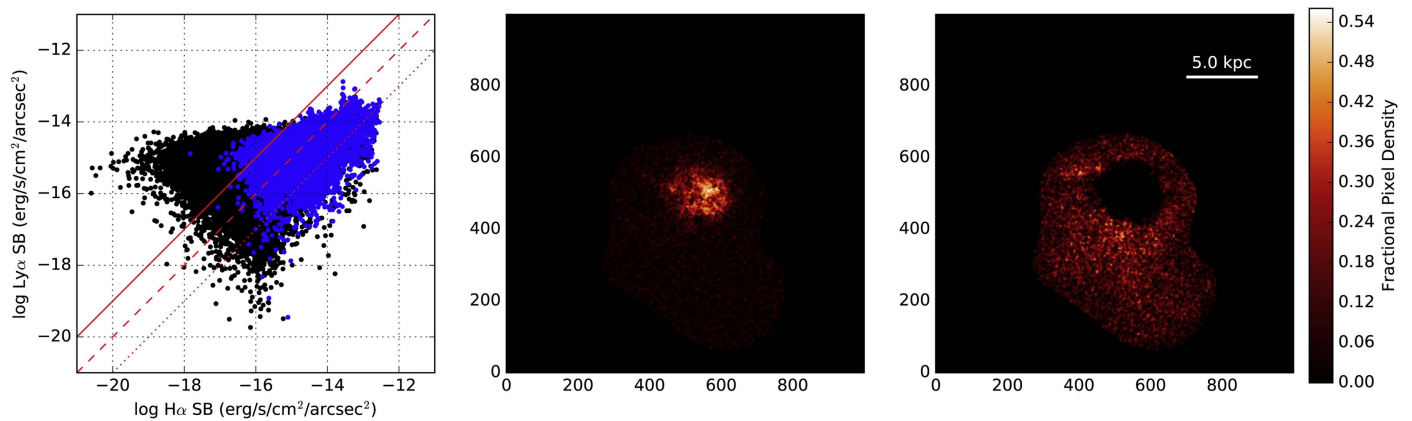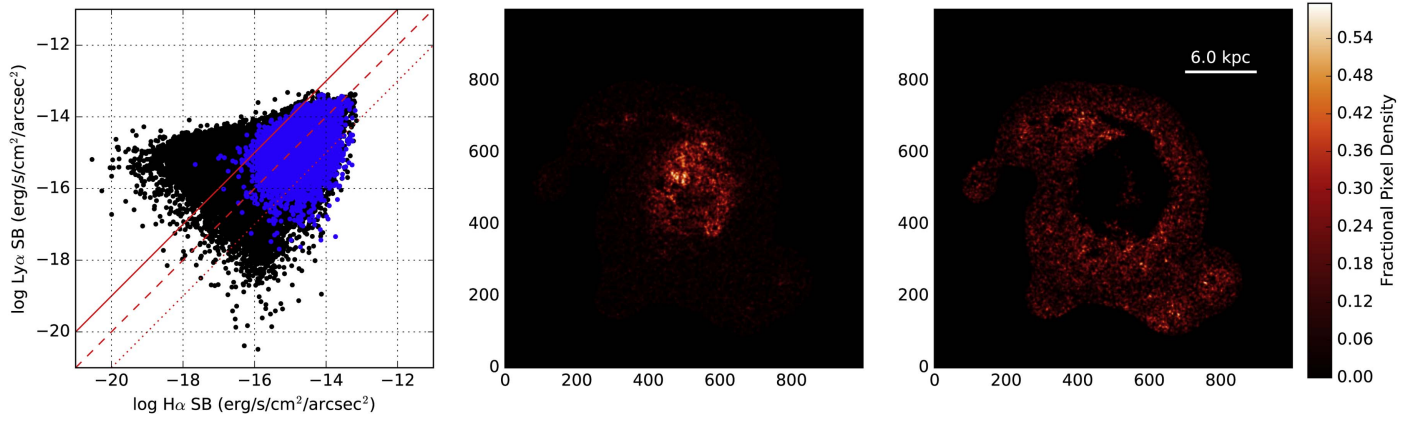

Figure 20. Same as Figure 6, but for LARS03.
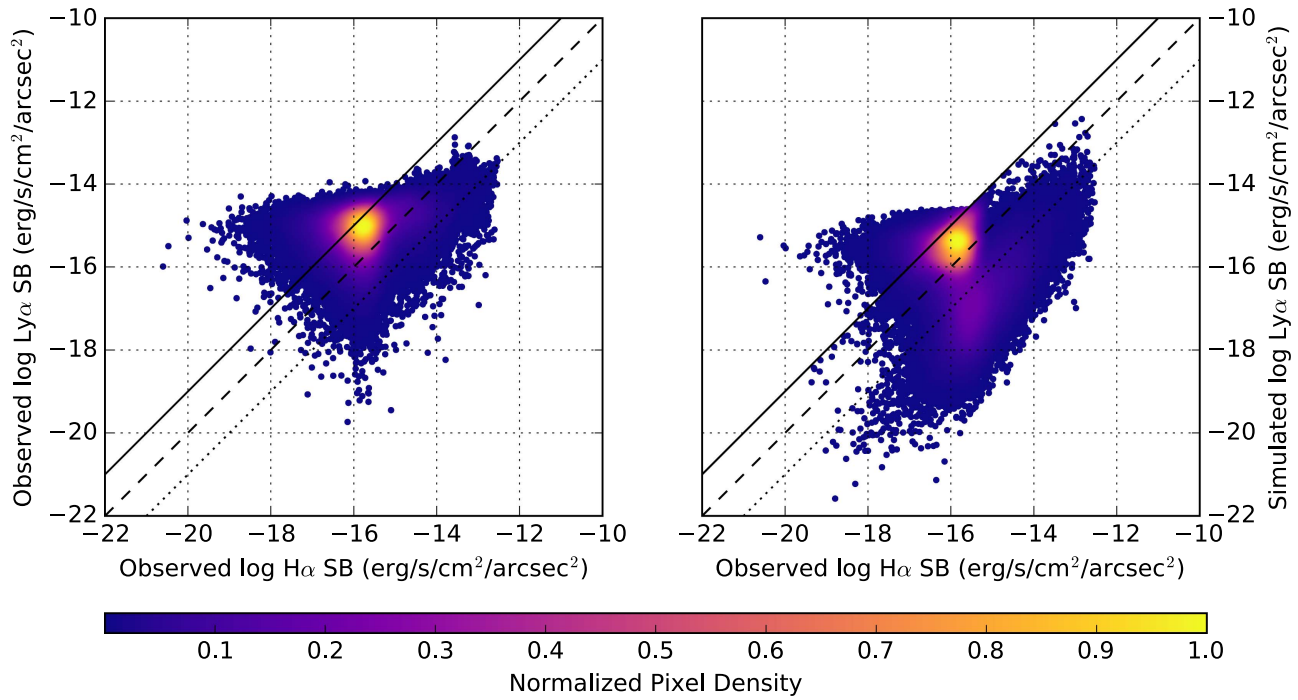
Figure 21. Same as Figure 8, but for LARS03.
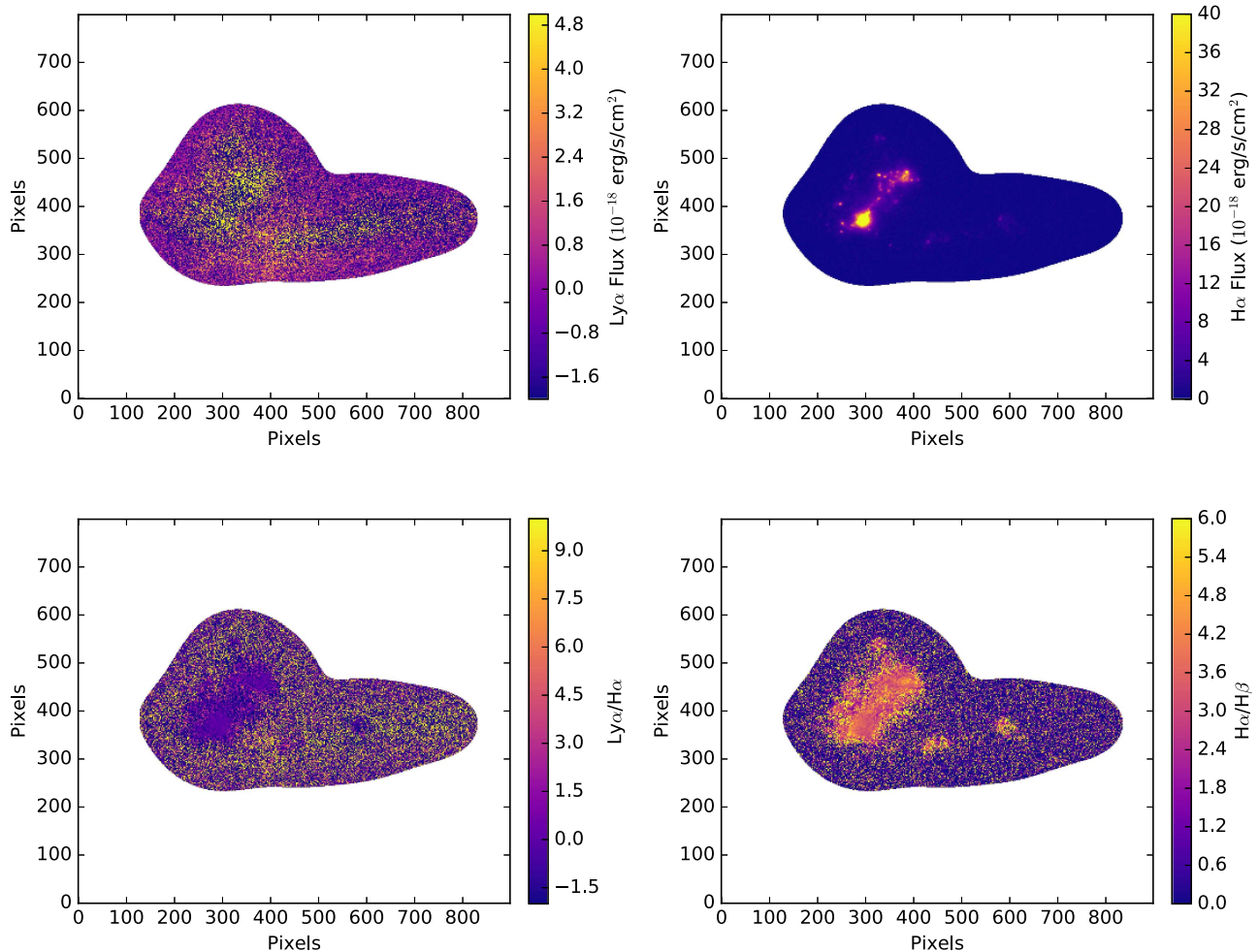
Figure 22. Images of LARS04. The calculated aperture has been applied. Top left: the Lyα emission map. Top right: the Hα emission map. Bottom left: the Lyα/Hα ratio, with an average uncertainty of 0.007. Bottom right: the Hα/Hβ ratio, 0.002.
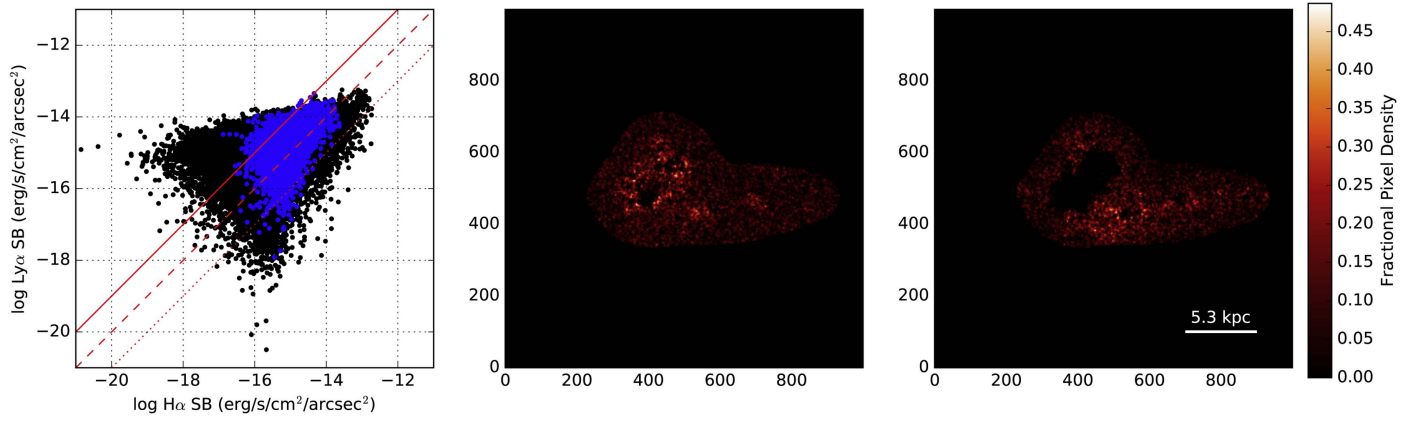
Figure 23. Same as Figure 6, but for LARS04.
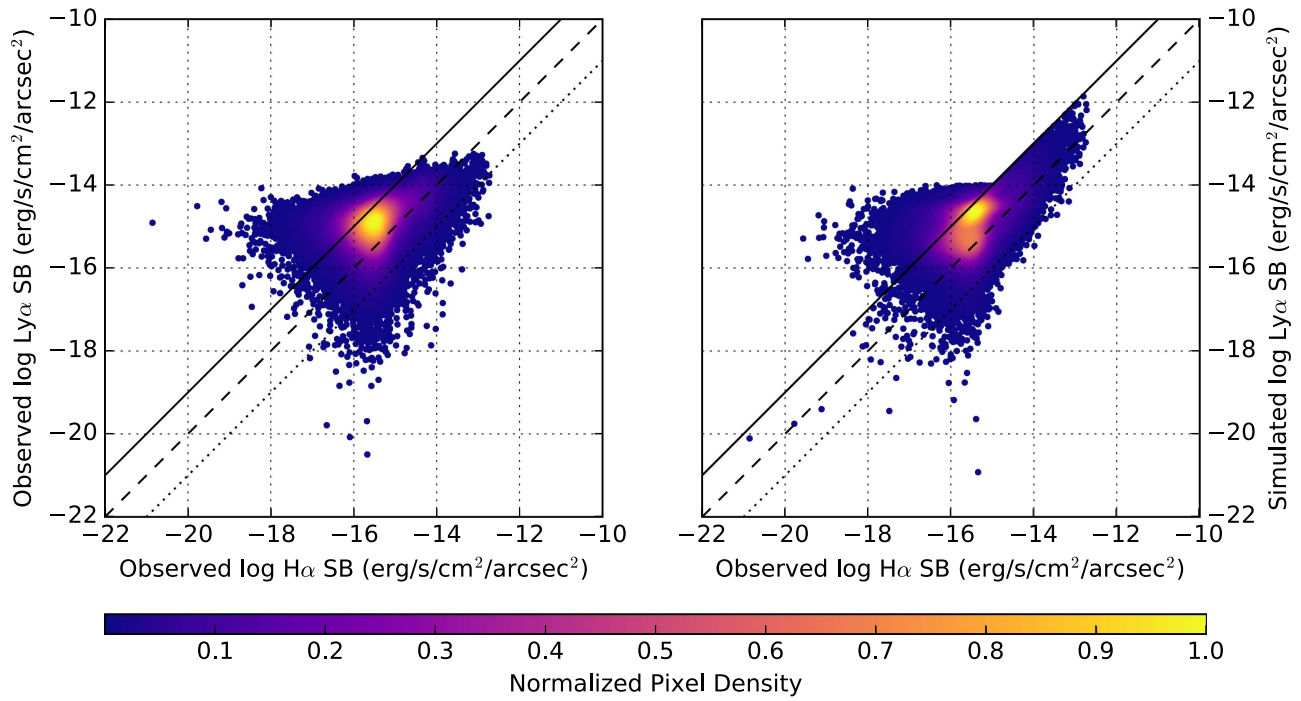
Figure 24. Same as Figure 8, but for LARS04.
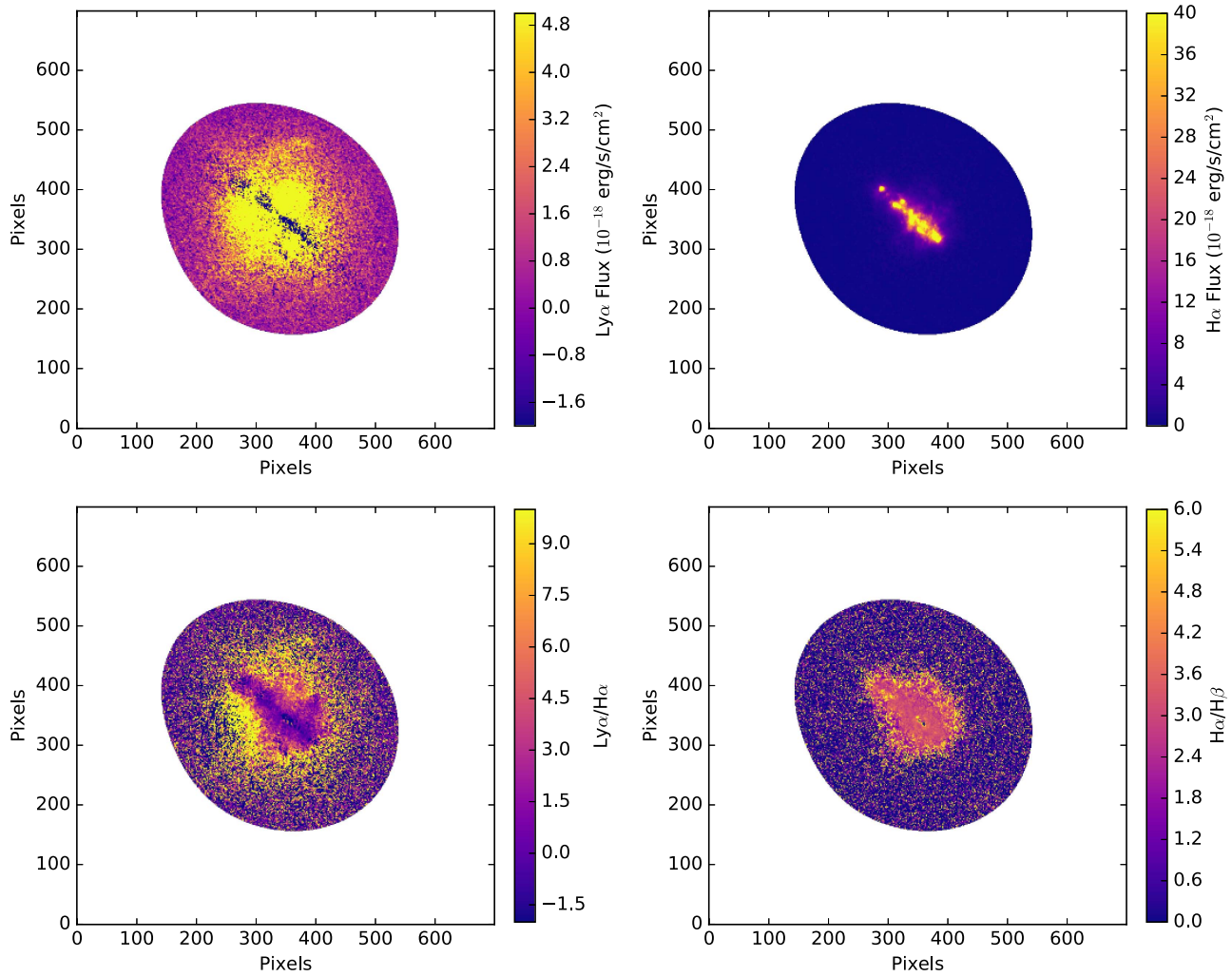
Figure 25. Images of LARS05. The calculated aperture has been applied. Top left: the Lyα emission map. Top right: the Hα emission map. Bottom left: the Lyα/Hα ratio, with an average uncertainty of 0.01. Bottom right: the Hα/Hβ ratio, with an average uncertainty of 0.002.

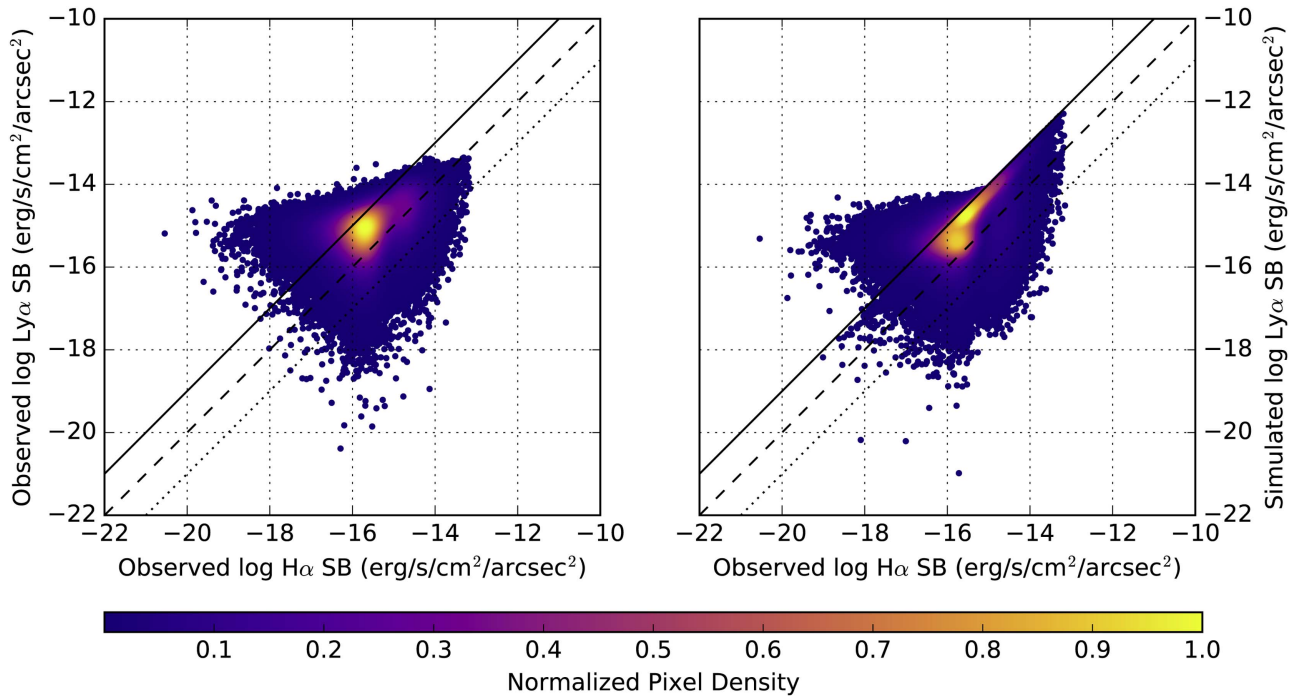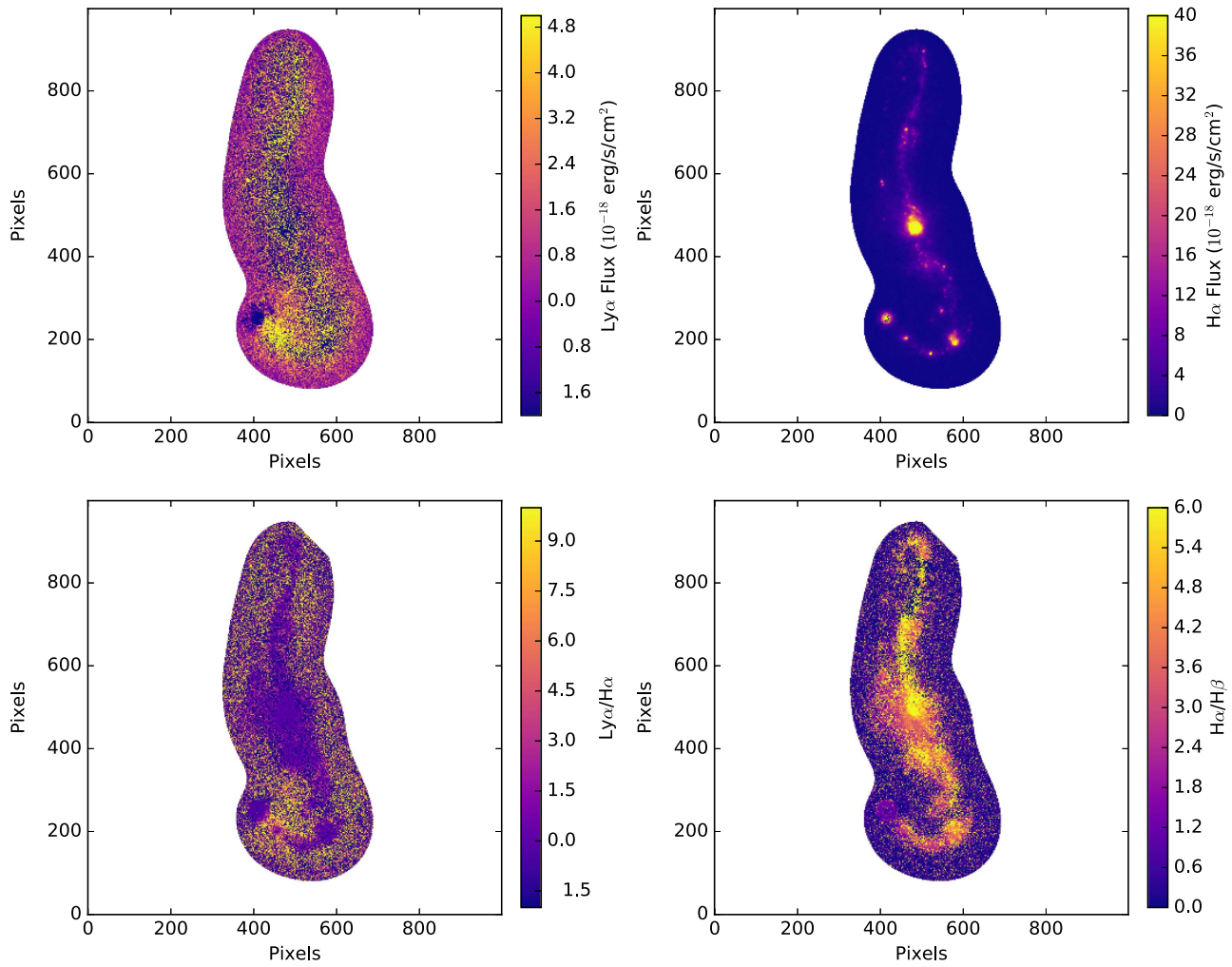**Figure 26.** Same as Figure 6, but for LARS05.

Figure 27. Same as Figure 8, but for LARS05.

Figure 28. Images of LARS06. The calculated aperture has been applied. Top left: the Lyα emission map. Top right: the Hα emission map. Bottom left: the Lyα/Hα ratio, with an average uncertainty of 0.02. Bottom right: the Hα/Hβ ratio, with an average uncertainty of 0.002.
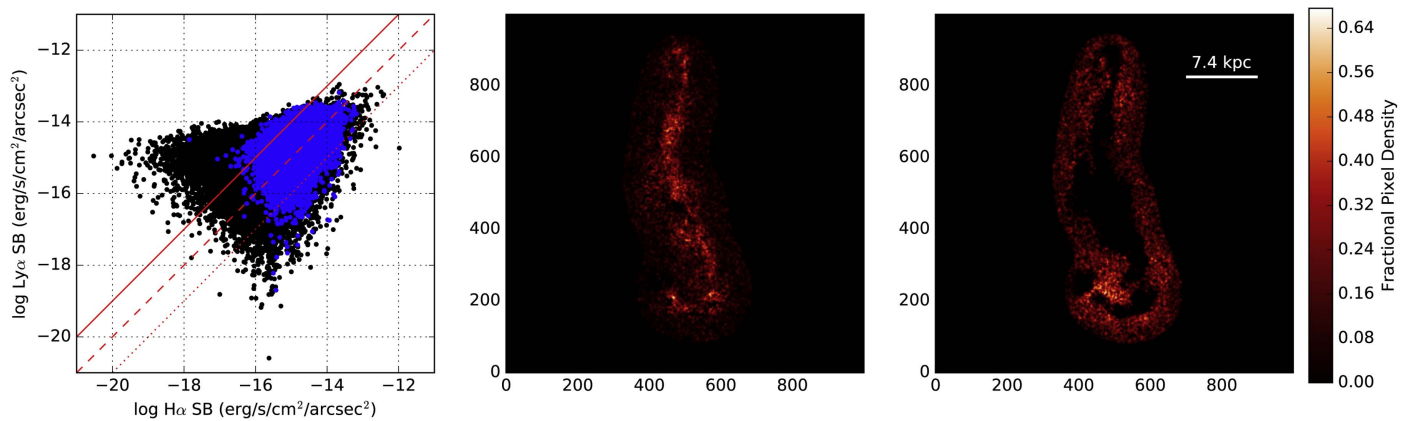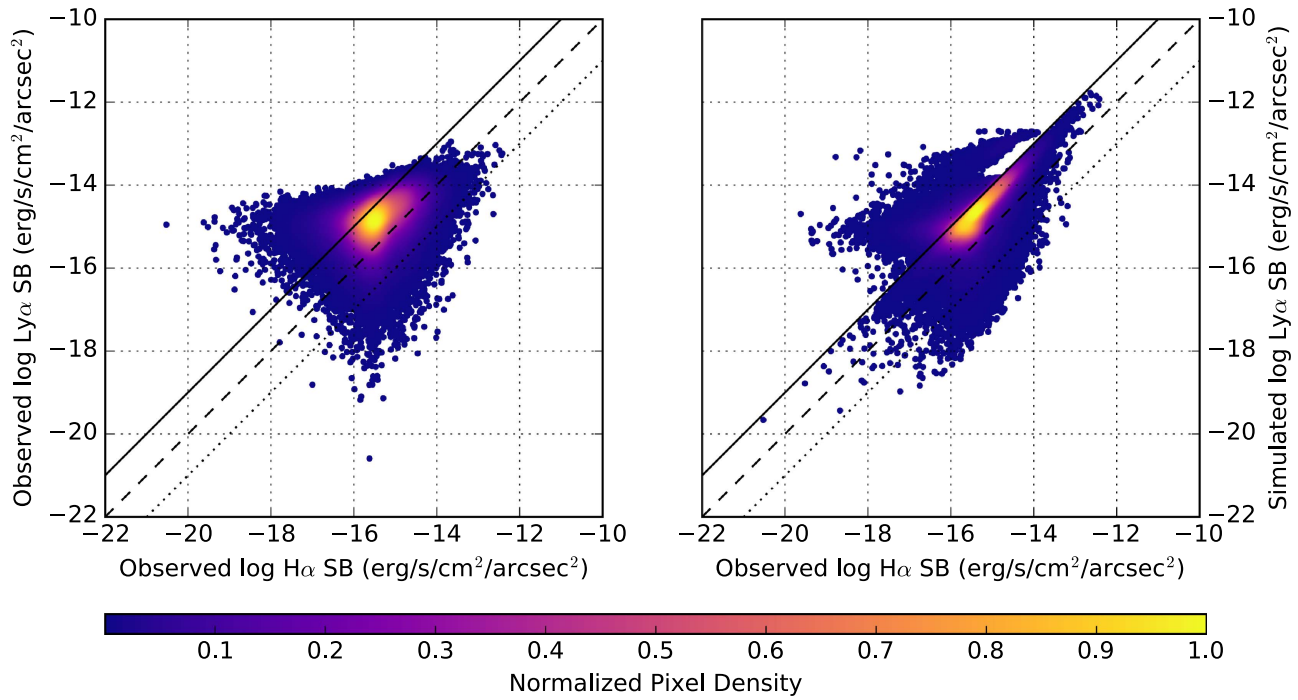
Figure 29. Same as Figure 6, but for LARS06.

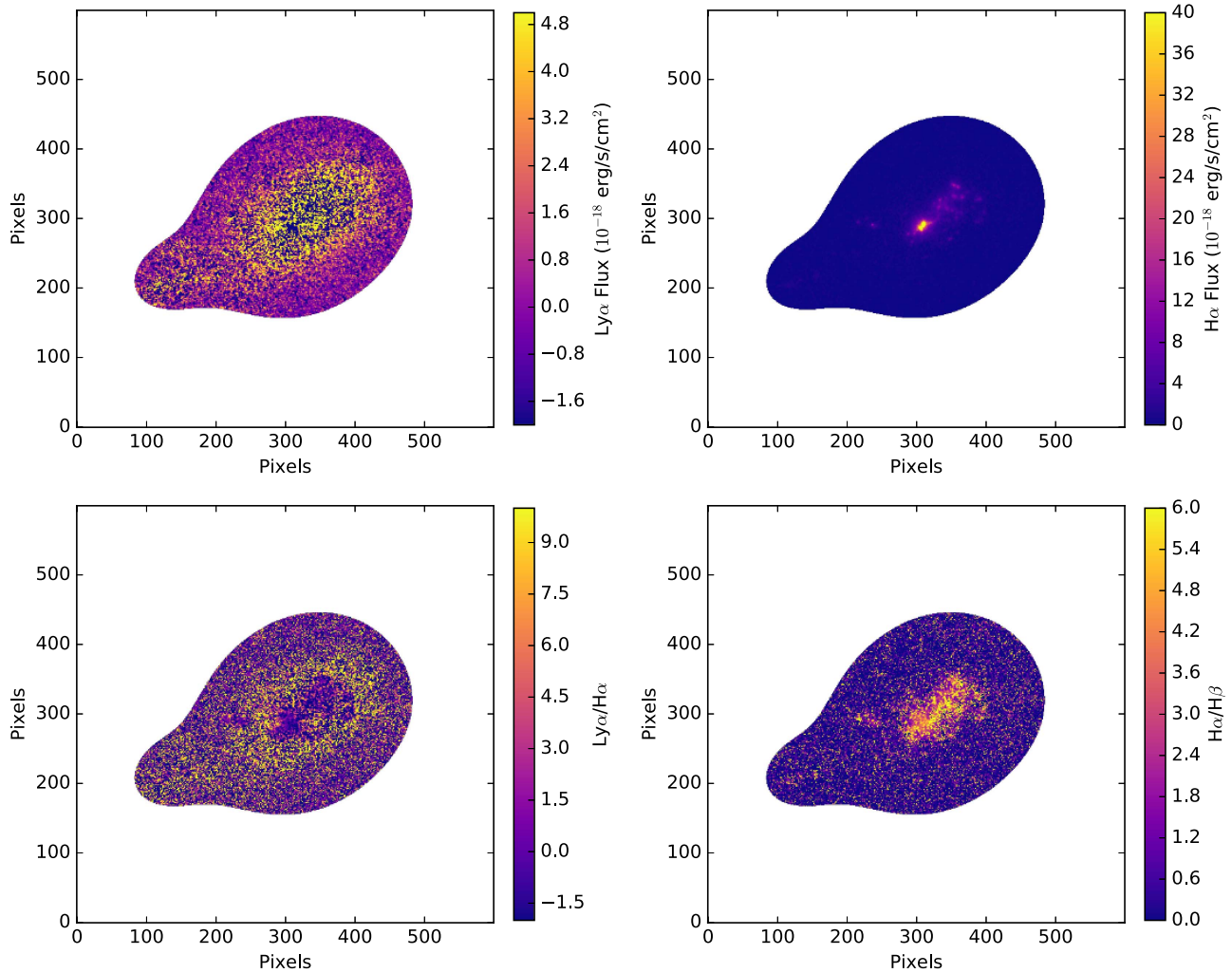**Figure 30.** Same as Figure 8, but for LARS06.

Figure 31. Images of LARS07. The calculated aperture has been applied. Top left: the Lyα emission map. Top right: the Hα emission map. Bottom left: the Lyα/Hα ratio, with an average uncertainty of 0.02. Bottom right: the Hα/Hβ ratio, with an average uncertainty of 0.003.
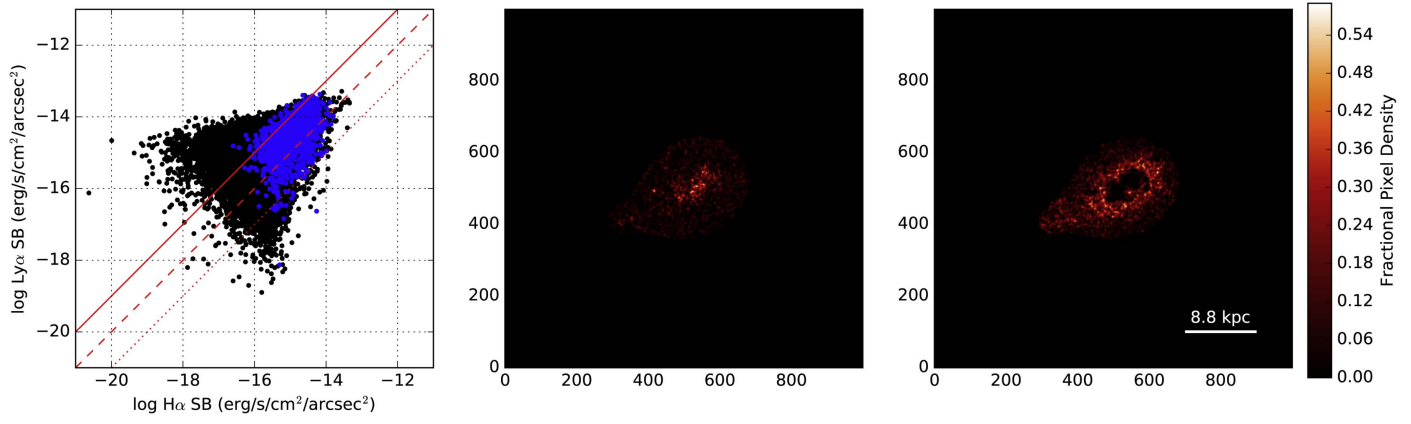

Figure 32. Same as Figure 6, but for LARS07.

Figure 33. Same as Figure 8, but for LARS07.

Figure 34. Images of LARS08. The calculated aperture has been applied. Top left: the Lyα emission map. Top right: the Hα emission map. Bottom left: the Lyα/Hα ratio, with an average uncertainty of 0.003. Bottom right: the Hα/Hβ ratio, with an average uncertainty of 0.007.

Figure 35. Same as Figure 6, but for LARS08.

Figure 36. Same as Figure 8, but for LARS08.

Figure 37. Images of LARS09. The calculated aperture has been applied. Top left: the Lyα emission map. Top right: the Hα emission map. Bottom left: the Lyα/Hα ratio, with an average uncertainty of 0.004. Bottom right: the Hα/Hβ ratio, with an average uncertainty of 0.002.
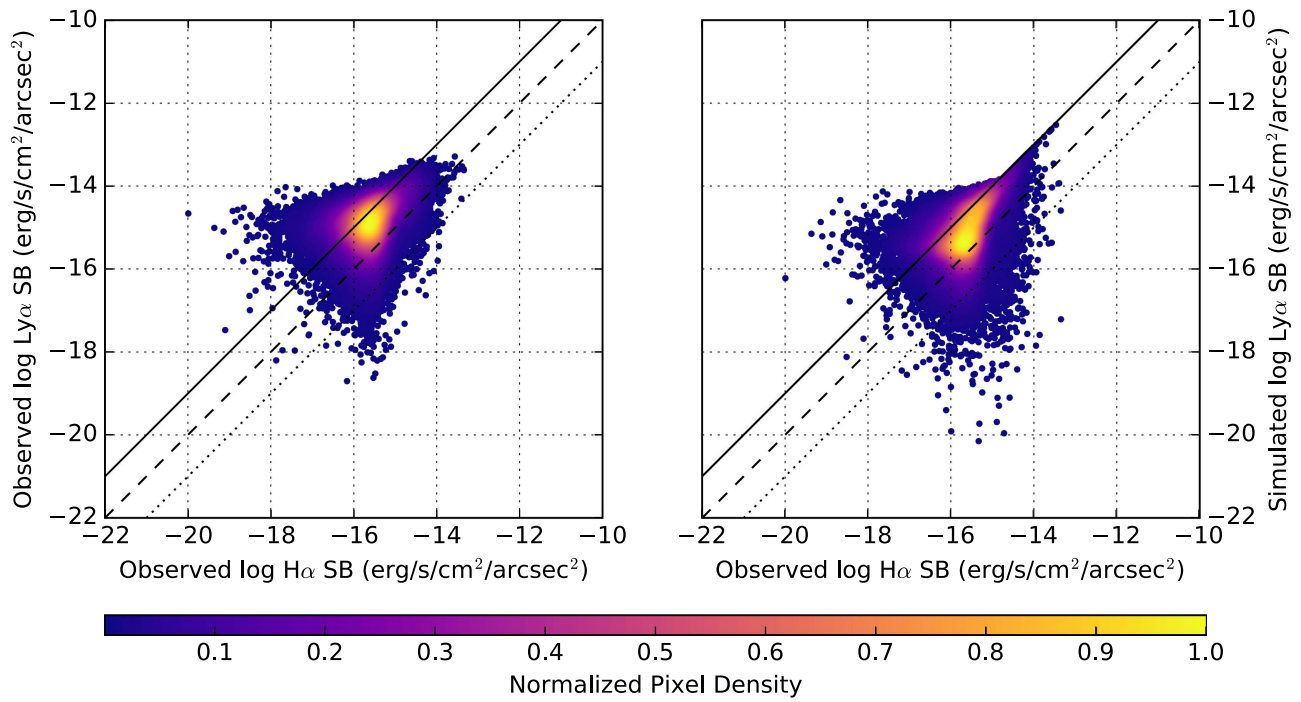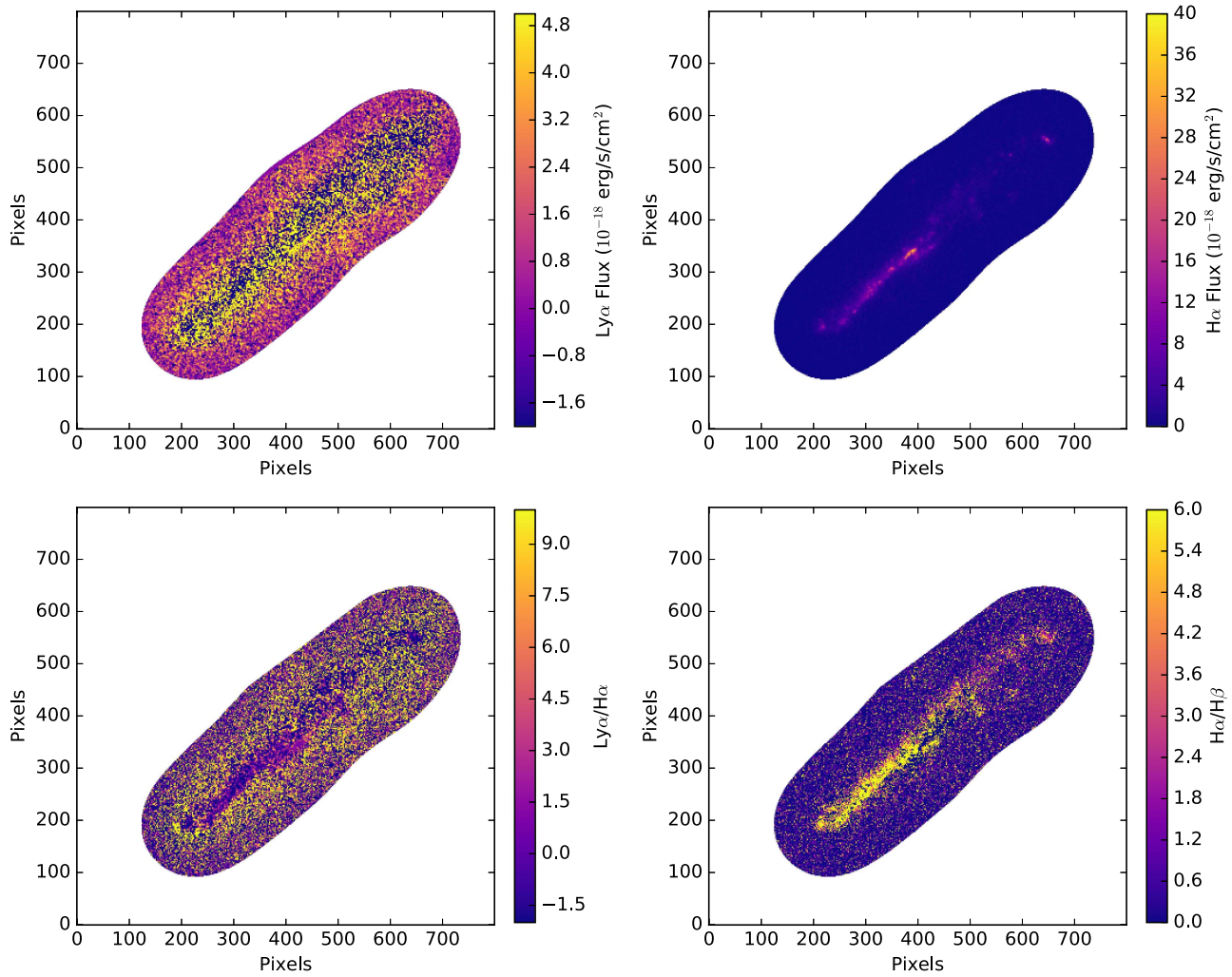

Figure 38. Same as Figure 6, but for LARS09.

Figure 39. Same as Figure 8, but for LARS09.

Figure 40. Images of LARS10. The calculated aperture has been applied. Top left: the Lyα emission map. Top right: the Hα emission map. Bottom left: the Lyα/Hα ratio, with an average uncertainty of 0.01. Bottom right: the Hα/Hβ ratio, with an average uncertainty of 0.003.
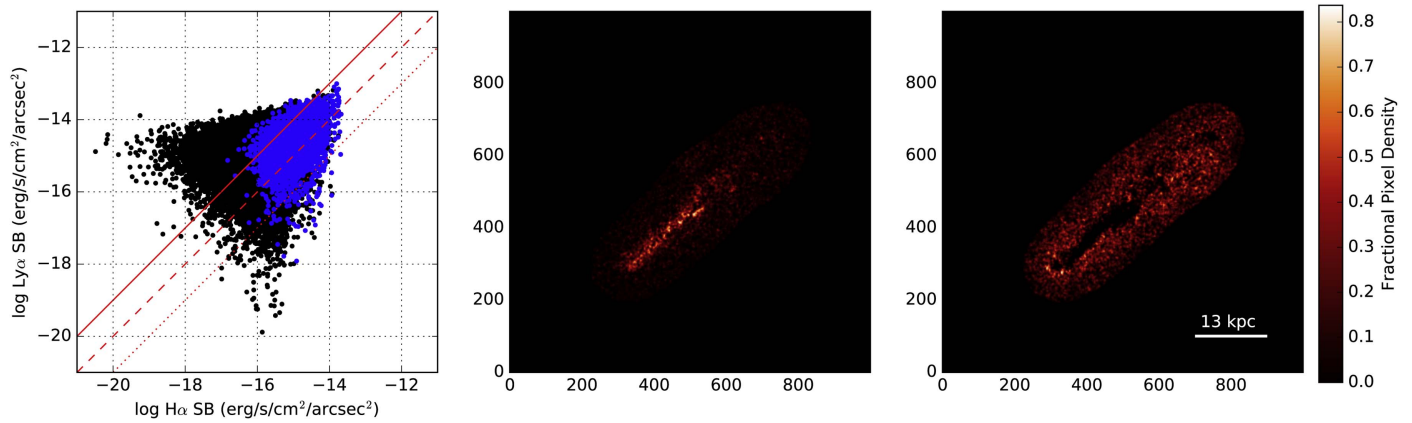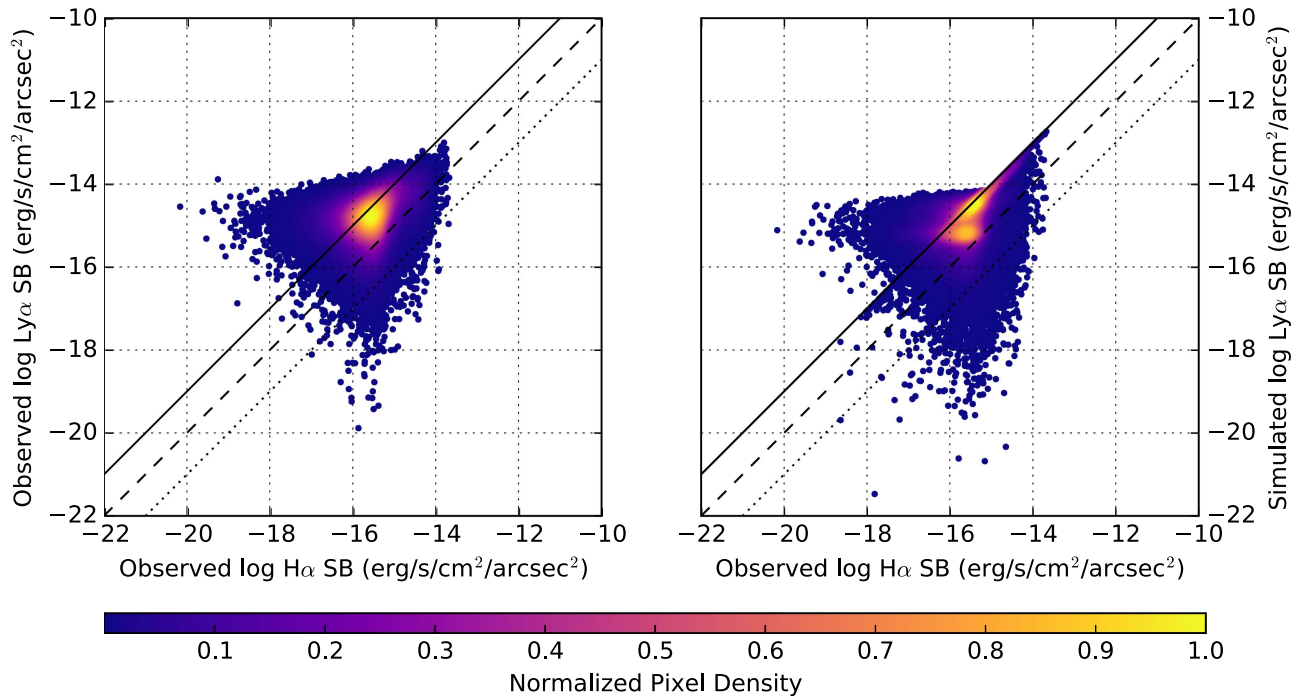
Figure 41. Same as Figure 6, but for LARS10.

Figure 42. Same as Figure 8, but for LARS10.

Figure 43. Images of LARS11. The calculated aperture has been applied. Top left: the Lyα emission map. Top right: the Hα emission map. Bottom left: the Lyα/Hα ratio, with an average uncertainty of 0.009. Bottom right: the Hα/Hβ ratio, with an average uncertainty of 0.01.

Figure 44. Same as Figure 6, but for LARS11.
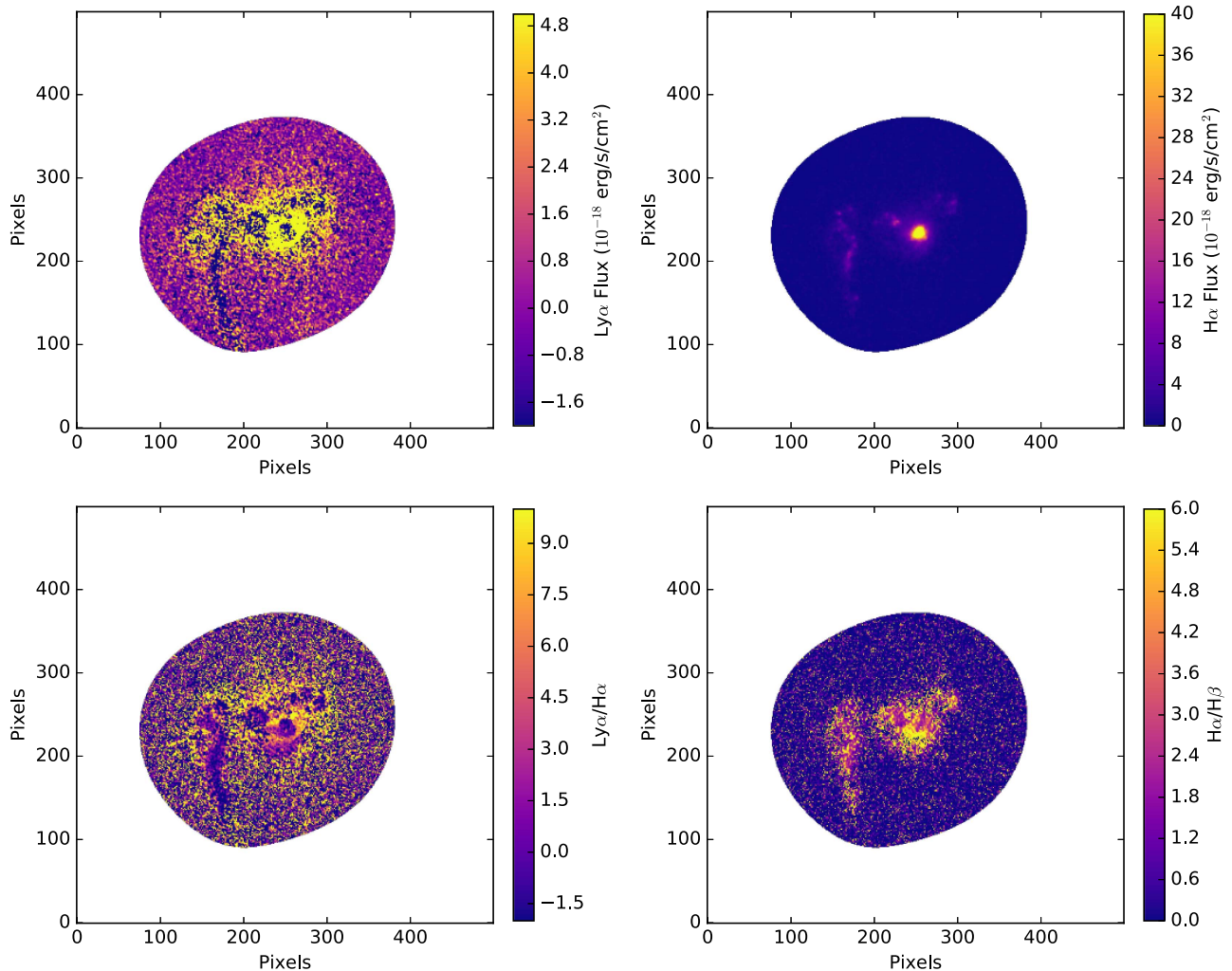
Figure 45. Same as Figure 8, but for LARS11.

Figure 46. Images of LARS13. The calculated aperture has been applied. Top left: the Lyα emission map. Top right: the Hα emission map. Bottom left: the Lyα/Hα ratio, with an average uncertainty of 0.07. Bottom right: the Hα/Hβ ratio, with an average uncertainty of 0.004.
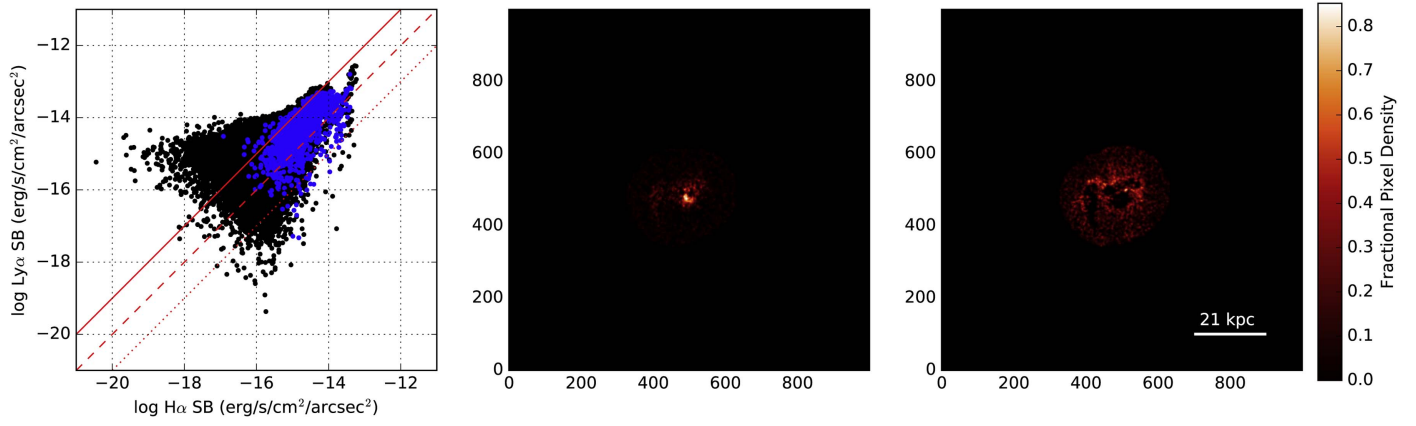
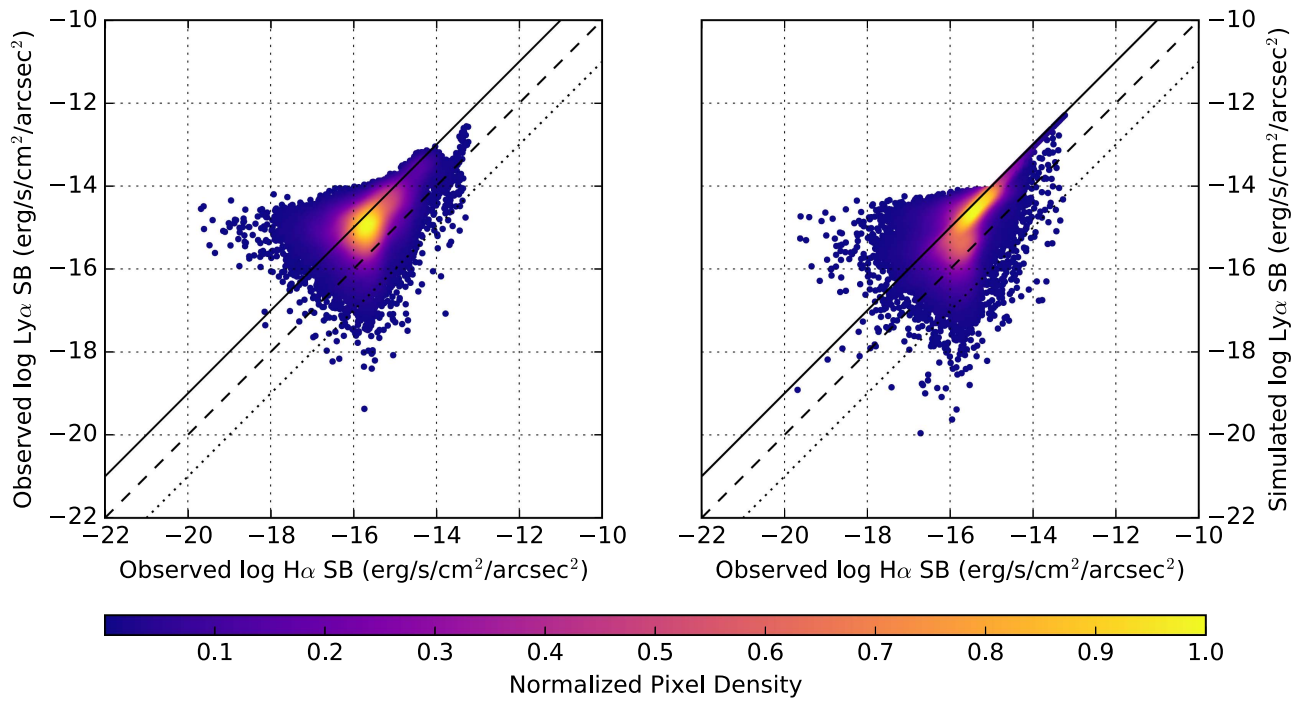**Figure 47.** Same as Figure 6, but for LARS13.

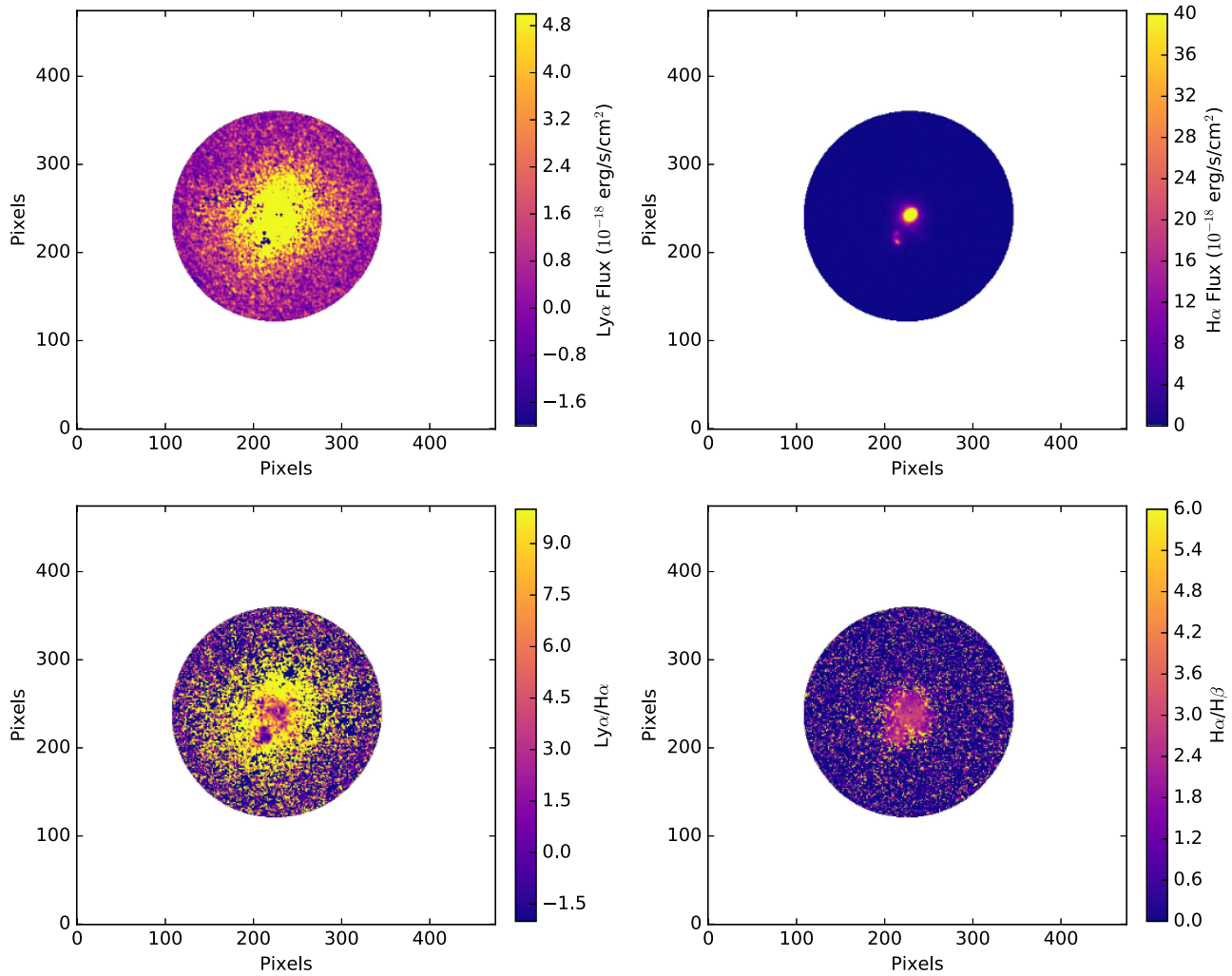**Figure 48.** Same as Figure 8, but for LARS13.

Figure 49. Images of LARS14. The calculated aperture has been applied. Top left: the Lyα emission map. Top right: the Hα emission map. Bottom left: the Lyα/Hα ratio, with an average uncertainty of 0.02. Bottom right: the Hα/Hβ ratio, with an average uncertainty of 0.002.
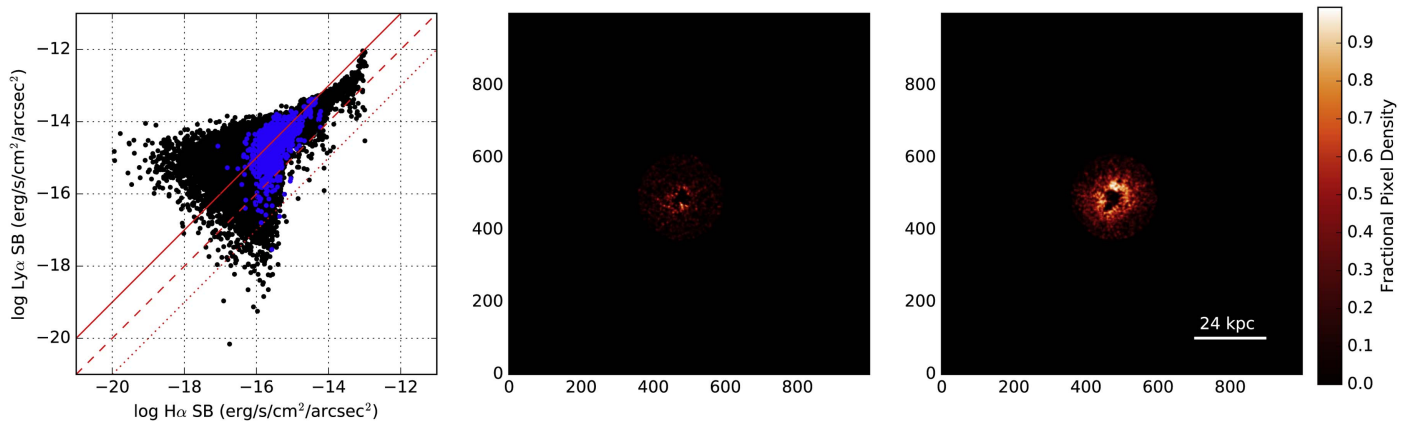

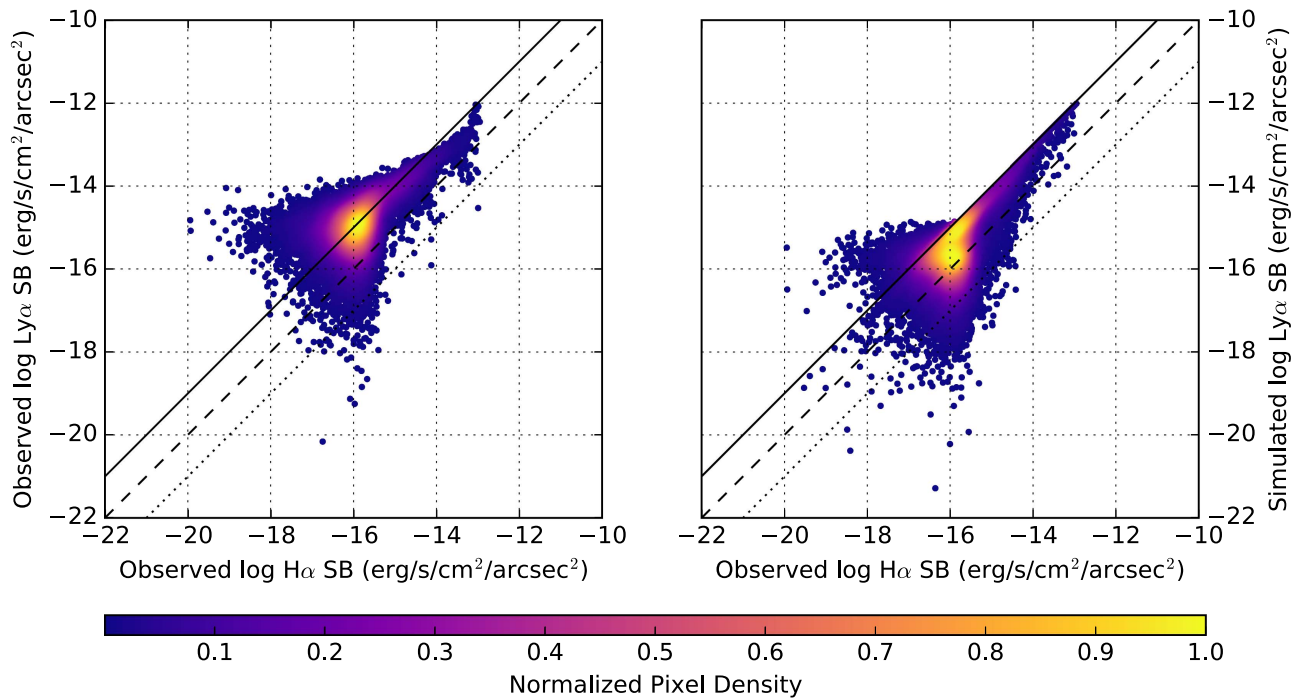**Figure 50.** Same as Figure 6, but for LARS14.

Figure 51. Same as Figure 8, but for LARS14.

ORCID iDs

Joanna S. Bridge ⓘ https://orcid.org/0000-0002-8584-1903
Matthew Hayes ⓘ https://orcid.org/0000-0001-8587-218X
Jens Melinder ⓘ https://orcid.org/0000-0003-0470-8754
Göran Östlin ⓘ https://orcid.org/0000-0002-3005-1349
Robin Ciardullo ⓘ https://orcid.org/0000-0002-1328-0211
Hakim Atek ⓘ https://orcid.org/0000-0002-7570-0824
John M. Cannon ⓘ https://orcid.org/0000-0002-1821-7019
Max Gronke ⓘ https://orcid.org/0000-0003-2491-060X
Lucia Guaita ⓘ https://orcid.org/0000-0002-4902-0075
Alex Hagen ⓘ https://orcid.org/0000-0003-2031-7737
Edmund Christian Herenz ⓘ https://orcid.org/0000-0002-8505-4678
Daniel Kunth ⓘ https://orcid.org/0000-0002-3635-0112
Peter Laursen ⓘ https://orcid.org/0000-0003-4207-0245
J. Miguel Mas-Hesse ⓘ https://orcid.org/0000-0002-8823-9723
Stephen A. Pardy ⓘ https://orcid.org/0000-0002-6856-1379

References

Adams, T. F. 1972, ApJ, 174, 439
Astropy Collaboration, Robitaille, T. P., Tollerud, E. J., et al. 2013, A&A, 558, A33
Atek, H., Kunth, D., Hayes, M., Östlin, G., & Mas-Hesse, J. M. 2008, A&A, 488, 491
Atek, H., Kunth, D., Schaerer, D., et al. 2014, A&A, 561, A89
Behrens, C., Dijkstra, M., & Niemeyer, J. C. 2014, A&A, 563, A77
Brocklehurst, M. 1971, MNRAS, 153, 471
Cardelli, J. A., Clayton, G. C., & Mathis, J. S. 1989, ApJ, 345, 245
Dijkstra, M. 2014, PASA, 31, e040
Duval, F., Östlin, G., Hayes, M., et al. 2016, A&A, 587, A77
Foreman-Mackey, D., Hogg, D. W., Lang, D., & Goodman, J. 2013, PASP, 125, 306
Gardner, J. P., Mather, J. C., Clampin, M., et al. 2006, SSRv, 123, 485

Giavalisco, M., Koratkar, A., & Calzetti, D. 1996, ApJ, 466, 831
Gronke, M., Bull, P., & Dijkstra, M. 2015, ApJ, 812, 123
Gronke, M., Dijkstra, M., McCourt, M., & Oh, S. P. 2016, ApJL, 833, L26
Gronke, M., Dijkstra, M., McCourt, M., & Oh, S. P. 2017, A&A, 607, A71
Guaita, L., Talia, M., Pentericci, L., et al. 2017, A&A, 606, A19
Hayes, M. 2015, PASA, 32, e027
Hayes, M., Melinder, J., Östlin, G., et al. 2016, ApJ, 828, 49
Hayes, M., Östlin, G., Atek, H., et al. 2007, MNRAS, 382, 1465
Hayes, M., Östlin, G., Duval, F., et al. 2014, ApJ, 782, 6
Hayes, M., Östlin, G., Mas-Hesse, J. M., et al. 2005, A&A, 438, 71
Hayes, M., Östlin, G., Mas-Hesse, J. M., & Kunth, D. 2009, AJ, 138, 911
Hayes, M., Östlin, G., Schaerer, D., et al. 2013, ApJL, 765, L27
Heckman, T. M., Borthakur, S., Overzier, R., et al. 2011, ApJ, 730, 5
Herenz, E. C., Gruyters, P., Orlitova, I., et al. 2016, A&A, 587, A78
Hill, G. J., Gebhardt, K., Komatsu, E., et al. 2008, in ASP Conf. Ser. 399, Panoramic Views of Galaxy Formation and Evolution, ed. T. Kodama, T. Yamada, & K. Aoki (San Francisco, CA: ASP), 115
Hu, E. M., Cowie, L. L., & McMahon, R. G. 1998, ApJL, 502, L99
Hummer, D. G., & Storey, P. J. 1987, MNRAS, 224, 801
Kennicutt, R. C., Jr. 1998, ARA&A, 36, 189
Komatsu, E., Smith, K. M., Dunkley, J., et al. 2011, ApJS, 192, 18
Kunth, D., Lequeux, J., Sargent, W. L. W., & Viallefond, F. 1994, A&A, 282, 709
Kunth, D., Mas-Hesse, J. M., Terlevich, E., et al. 1998, A&A, 334, 11
Laursen, P., Duval, F., & Östlin, G. 2013, ApJ, 766, 124
Laursen, P., Sommer-Larsen, J., & Andersen, A. C. 2009, ApJ, 704, 1640
Leitherer, C., Schaerer, D., Goldader, J. D., et al. 1999, ApJS, 123, 3
Lequeux, J., Kunth, D., Mas-Hesse, J. M., & Sargent, W. L. W. 1995, A&A, 301, 18
Mas-Hesse, J. M., Kunth, D., Tenorio-Tagle, G., et al. 2003, ApJ, 598, 858
Mathis, J. S. 1972, ApJ, 176, 651
Muna, D., Alexander, M., Allen, A., et al. 2016, arXiv:1610.03159
Natta, A., & Panagia, N. 1984, ApJ, 287, 228
Neufeld, D. A. 1990, ApJ, 350, 216
Östlin, G., Hayes, M., Duval, F., et al. 2014, ApJ, 797, 11
Östlin, G., Hayes, M., Kunth, D., et al. 2009, AJ, 138, 923
Pardy, S. A., Cannon, J. M., Östlin, G., et al. 2014, ApJ, 794, 101
Partridge, R. B., & Peebles, P. J. E. 1967, ApJ, 147, 868
Pengelly, R. M. 1964, MNRAS, 127, 145

Petrosian, V. 1976, ApJL, 209, L1
Raiter, A., Schaerer, D., & Fosbury, R. A. E. 2010, A&A, 523, A64
Rivera-Thorsen, T. E., Hayes, M., Östlin, G., et al. 2015, ApJ, 805, 14
Scarlata, C., Colbert, J., Teplitz, H. I., et al. 2009, ApJL, 704, L98
Spearman, C. 1904, Am. J. Psychol., 15, 72
Spitzer, L. 1978, Physical Processes in the Interstellar Medium (New York: Wiley)

Tenorio-Tagle, G., Silich, S. A., Kunth, D., Terlevich, E., & Terlevich, R. 1999, MNRAS, 309, 332
Terlevich, E., Diaz, A. I., Terlevich, R., & Vargas, M. L. G. 1993, MNRAS, 260, 3
Verhamme, A., Schaerer, D., Atek, H., & Tapken, C. 2008, A&A, 491, 89
Verhamme, A., Schaerer, D., & Maselli, A. 2006, A&A, 460, 397
Vijh, U. P., Witt, A. N., & Gordon, K. D. 2003, ApJ, 587, 533
Wofford, A., Leitherer, C., & Salzer, J. 2013, ApJ, 765, 118